LETTERS
PUBLISHED ONLINE: 2 FEBRUARY 2015 | DOI: 10.1038/NNANO.2015.1
nature nanotechnology

Asymmetric dyes align inside carbon nanotubes to yield a large nonlinear optical response

Sofie Cambré[1†], Jochen Campo[1†], Charlie Beirnaert[1], Christof Verlackt[1], Pegie Cool[2] and Wim Wenseleers[1*]

Asymmetric dye molecules have unusual optical and electronic properties[1–3]. For instance, they show a strong second-order nonlinear optical (NLO) response that has attracted great interest for potential applications in electro-optic modulators for optical telecommunications and in wavelength conversion of lasers[2,3]. However, the strong Coulombic interaction between the large dipole moments of these molecules favours a pairwise antiparallel alignment that cancels out the NLO response when incorporated into bulk materials. Here, we show that by including an elongated dipolar dye (*p*,*p*′-dimethylaminonitrostilbene, DANS, a prototypical asymmetric dye with a strong NLO response[4]) inside single-walled carbon nanotubes (SWCNTs)[5,6], an ideal head-to-tail alignment in which all electric dipoles point in the same sense is naturally created. We have applied this concept to synthesize solution-processible DANS-filled SWCNTs that show an extremely large total dipole moment and static hyperpolarizability ($\beta_0 = 9{,}800 \times 10^{-30}$ e.s.u.), resulting from the coherent alignment of arrays of ~70 DANS molecules.

Encapsulating molecules inside SWCNTs is a common strategy to add new functionalities[7–9]. Here, we exploit the one-dimensional nature of SWCNTs' internal channels to induce molecular order that leads to an enhancement of the NLO response. At the molecular level, a large NLO response (expressed by the hyperpolarizability β) is typically achieved by combining the highly polarizable backbone of a conjugated molecule with the necessary asymmetry induced by substitution with electron-donating and -accepting groups at opposite ends. Compared to the currently widely used inorganic crystals such as lithium niobate, the NLO response of such organic molecules is intrinsically stronger and faster, and they also promise cheaper, solution-based processing, but their mutually parallel alignment is an important issue. Very exceptionally, specific (and rather unpredictable) intermolecular interactions result in suitable, non-centrosymmetric crystals[10] or J-aggregates[11], but for the vast majority of efficient NLO chromophores, dipole–dipole interactions dominate, resulting in a pairwise, side-by-side antiparallel alignment. Therefore, suitable parallel alignment is instead typically pursued by electric-field poling of the dipolar molecules in a heated polymer film[12], but this intrinsically results in a thermodynamically unstable state, and long-term degradation of the orientation remains a problem. In contrast, in one dimension the desired supramolecular head-to-tail alignment is expected to occur in thermodynamic equilibrium (Fig. 1 and Supplementary Section 6).

Dye-filled SWCNTs (*p*,*p*′-dimethylaminonitrostilbene (DANS)@oSWCNT, where the prefix 'o' refers to opened SWCNTs as opposed to pristine, end-capped SWCNTs, and '@' refers to filling) were synthesized using SWCNTs with different diameter ranges (see Methods). Although the synthesis is straightforward, characterization of these complex materials and the obtained alignment requires an extensive combination of spectroscopic information. A first indication of the encapsulation is obtained from optical absorption spectra (Fig. 2a–c). Besides the typical series of SWCNT absorption bands[13], the DANS@oSWCNT samples show an additional absorption band around 500 nm, corresponding to the dye molecules, which is not observed for analogous samples synthesized starting from closed SWCNTs (Supplementary Fig. 3). It also shows a pronounced redshift compared to free DANS molecules in solution (Fig. 2c), which is consistent with the envisaged head-to-tail coupling of the dipolar molecules, stabilizing the

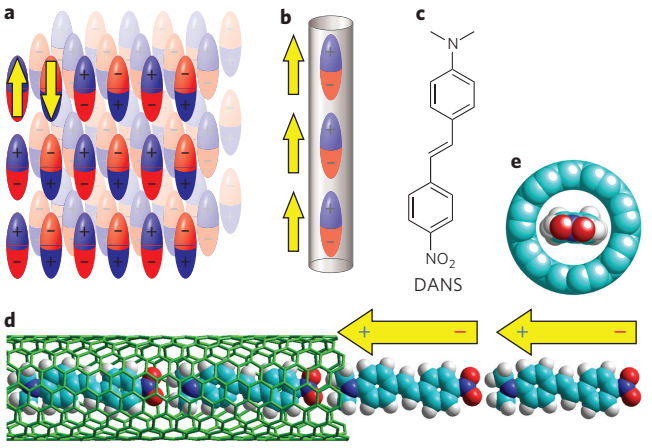

Figure 1 | Stacking of dipolar molecules in different dimensions. a, In two- or three-dimensional bulk materials, Coulomb interactions tend to favour a pairwise antiparallel ordering, thus cancelling asymmetric properties such as the NLO response. **b**, In one-dimensional confinement, a polar head-to-tail order is naturally favoured, as oppositely charged 'heads' and 'tails' attract each other, leading to a constructive addition of the molecular NLO responses (and dipole moments). **c**, Chemical structure of *p*,*p*′-dimethylaminonitrostilbene (DANS), a prototypical NLO molecule. **d**, Theoretical model (optimized at the Hartree–Fock level with the semi-empirical AM1[30] Hamiltonian) of these NLO molecules in a (9,7) single-walled carbon nanotube (diameter, 1.09 nm), showing that the internal channel just fits a single file of molecules (for clarity the SWCNT is represented by a thin wire frame and partially removed, and two dye molecules are continued periodically outside the nanotube). **e**, Axial view of the same structure, with all atoms represented with their van der Waals radii, showing more clearly the relative size of DANS molecules and the SWCNT internal channel.

[1]Physics Department, University of Antwerp, Universiteitsplein 1, B-2610 Antwerp, Belgium. [2]Laboratory of Adsorption and Catalysis, Chemistry Department, University of Antwerp, Universiteitsplein 1, B-2610 Antwerp, Belgium. †These authors contributed equally to this work.
*e-mail: wim.wenseleers@uantwerp.be

zwitterionic excited state of the DANS[14]. Indeed, a simple model shows that the electric field of the neighbouring dipoles in the one-dimensional array acting on a given DANS molecule is oriented in the same sense and of even larger magnitude than the reaction field of a very polar solvent (Supplementary Section 7).

The encapsulation of the dye also influences the electronic transitions of the SWCNTs (both semiconducting and metallic). The absorption peaks of the largest-diameter (longest absorption wavelength) SWCNTs are blueshifted and narrowed relative to the corresponding oSWCNT solutions, which are water-filled[15–18] (D_2O@oSWCNT, Fig. 2a,b; also relative to solvent-filled SWCNTs: Supplementary Fig. 4). However, they are still redshifted and slightly broadened compared to the empty, closed SWCNTs (Supplementary Fig. 4). This is consistent with DANS encapsulation occurring in these larger-diameter SWCNTs, preventing water from entering and hence eliminating the large inhomogeneous broadening and dielectric screening induced redshift[18] associated with water filling.

Using infrared photoluminescence-excitation (PLE) spectroscopy, which resolves each individual type of semiconducting SWCNT[13] (with their diameters and chiral structures indicated by their chiral indices (n,m)), more detailed information on the encapsulation and its effect on the electronic transitions of the SWCNTs is obtained (Fig. 2d–i). The PLE peaks of each of the DANS@oSWCNTs show a shift (see below and Fig. 3) and narrowing of both the E_{11} (bandgap emission) and E_{22} (excitation) transitions relative to the water-filled reference sample D_2O@oSWCNTs (Fig. 2d,e; see Supplementary Section 3 for other samples). Moreover, an additional band located at the excitation wavelength of the dye but at the emission wavelengths of the SWCNTs (Fig. 2f–i and Supplementary Figs 7–9) demonstrates energy transfer from the dye to the SWCNTs, direct proof of a close interaction between both. The high efficiency of this energy transfer is illustrated by a nearly complete quenching of the DANS molecules' own fluorescence (Supplementary Section 3f). This energy-transfer band is more clearly visualized after proper normalization over and subtraction of the pure SWCNT PLE signals (Fig. 2f–h) and shows a quite sharp onset at an emission wavelength of ~1,350 nm (Fig. 2g,h), a strong indication of a critical diameter for filling: the thinnest tubes for which the energy-transfer band is observed are the (9,7) and/or (13,2) SWCNTs (whose emissions coincide, Supplementary Fig. 7), corresponding to a minimum encapsulation diameter of 1.08–1.1 nm. The dye excitation profile shows subtle variations with nanotube diameter (emission wavelength; Fig. 2h, Supplementary Fig. 7), indicating slight differences in the molecular stacking in different SWCNTs. The integrated excitation profile of this energy transfer band is also in good agreement with the absorption data (Fig. 2i).

To accurately determine the SWCNT PLE peak positions and linewidths for each individual chirality and their changes upon filling, a two-dimensional fitting procedure was developed (Supplementary Section 3e, Supplementary Fig. 10). The results show that for small-diameter tubes up to the (8,7) chirality (that is, $d \leq 1.02$ nm), DANS molecules are not encapsulated, as no differences are observed between the DANS@oSWCNT and solvent@oSWCNT samples (Fig. 3a), while for larger diameters, the electronic transitions are clearly shifted. Most SWCNTs reveal a redshift with respect to the solvent-filled tubes (and with respect to the D_2O-filled SWCNTs; Supplementary Fig. 11) and thus an even larger shift compared to the empty tubes, indicating a stronger interaction of the SWCNT excitons with the highly dipolar and highly polarizable DANS molecules. Note that the DANS dipoles are forced to be nearly parallel to the tube axis, while water molecules have larger orientational freedom, which also explains the larger inhomogeneous broadening for water-filled SWCNTs[18]. For SWCNTs with diameters between 1.02 and 1.08 nm, the PLE shifts indicate DANS-encapsulation, but Raman experiments (discussed in the following) show that this filling is only partial.

High-resolution resonant Raman spectroscopy is even more sensitive to the presence of molecules inside the SWCNTs. We have shown previously that the radial breathing modes (RBMs) of SWCNTs shift to higher frequencies upon water filling and that (unlike the electronic transitions) the RBMs of empty and water-filled SWCNTs can even be resolved in mixed samples, allowing the fraction of filled tubes to be quantified[15,17]. For the DANS@oSWCNT samples we find RBMs with yet another frequency, which is associated with DANS-filled SWCNTs, starting from the (9,7) tube (that is, $d \geq 1.08$ nm; Fig. 3b–d), in perfect agreement with the PLE results. For most chiralities this RBM of DANS-filled SWCNTs is shifted to even higher frequencies than the RBMs for water- or solvent-filled SWCNTs. For diameters near the threshold for filling (1.02 nm < d < 1.08 nm; for example, the (10,5) tube, Fig. 3b) a clear difference is observed between the solvent@oSWCNT and DANS@oSWCNT Raman spectra (as well as between their PLE spectra), but fitting the Raman spectra shows that only a fraction of these tubes are DANS-filled, while others are water-filled (Supplementary Figs 12–16). Thus, DANS molecules fit in SWCNTs with $d \geq 1.02$ nm, but whether filling actually occurs for $d < 1.08$ nm may still depend on the exact structure of the tube ends. The relative amplitudes of the RBM peaks corresponding to empty, water- or solvent-filled and DANS-filled SWCNTs also allow the fraction of DANS-filled SWCNTs to be estimated for each chirality, which is close to 100% for most chiralities (96% on average for diameters ≥ 1.1 nm; Supplementary Section 4). A high filling efficiency (≳70%) is also indicated by thermogravimetric and elemental analysis (Supplementary Section 1f).

Having established that the encapsulation was successful, the ultimate test of whether the molecules had indeed adopted the envisaged head-to-tail alignment and whether the DANS-filled SWCNTs indeed showed an enhanced NLO response was to measure the NLO polarizability (hyperpolarizability β) by second-harmonic light scattering (hyper-Rayleigh scattering, HRS[19]) from the DANS@oSWCNT solutions. Total DANS concentrations were calibrated based on the absorption data (Supplementary Sections 2 and 5a). For a solution of free dye molecules, HRS is a fully incoherent process and the intensities of N individual (randomly oriented) molecules simply add up linearly[19]:

$$I_{2\omega} \propto N\langle\beta^2\rangle I_\omega^2 \tag{1}$$

where $\langle\beta^2\rangle$ is an orientational average of the appropriate β components, I_ω is the incident fundamental laser intensity, and $I_{2\omega}$ is the total second-harmonic intensity. If the same number of dye molecules are grouped in arrays of n head-to-tail aligned molecules (with unchanged hyperpolarizability β of the individual molecules), the second-harmonic field amplitudes of molecules within one array add up coherently (hence intensity increases quadratically with n), while the resulting intensities of different arrays (randomly oriented in solution) add up incoherently,

$$\begin{aligned} I_{2\omega} &\propto \frac{N}{n}\langle(n\beta)^2\rangle I_\omega^2 \\ &\propto nN\langle\beta^2\rangle I_\omega^2 \end{aligned} \tag{2}$$

that is, an n times higher second-harmonic intensity is generated by the same total number of molecules. The extremely sensitive wavelength-dependent HRS set-up[20] used allows the NLO response to be measured throughout and beyond its resonance associated with the DANS absorption band (Fig. 4; also confirming DANS as the origin of the nonlinearity, as opposed to the SWCNTs themselves, which show a non-zero[21], but much smaller NLO response, Supplementary Section 5). Combined with an adequate dispersion

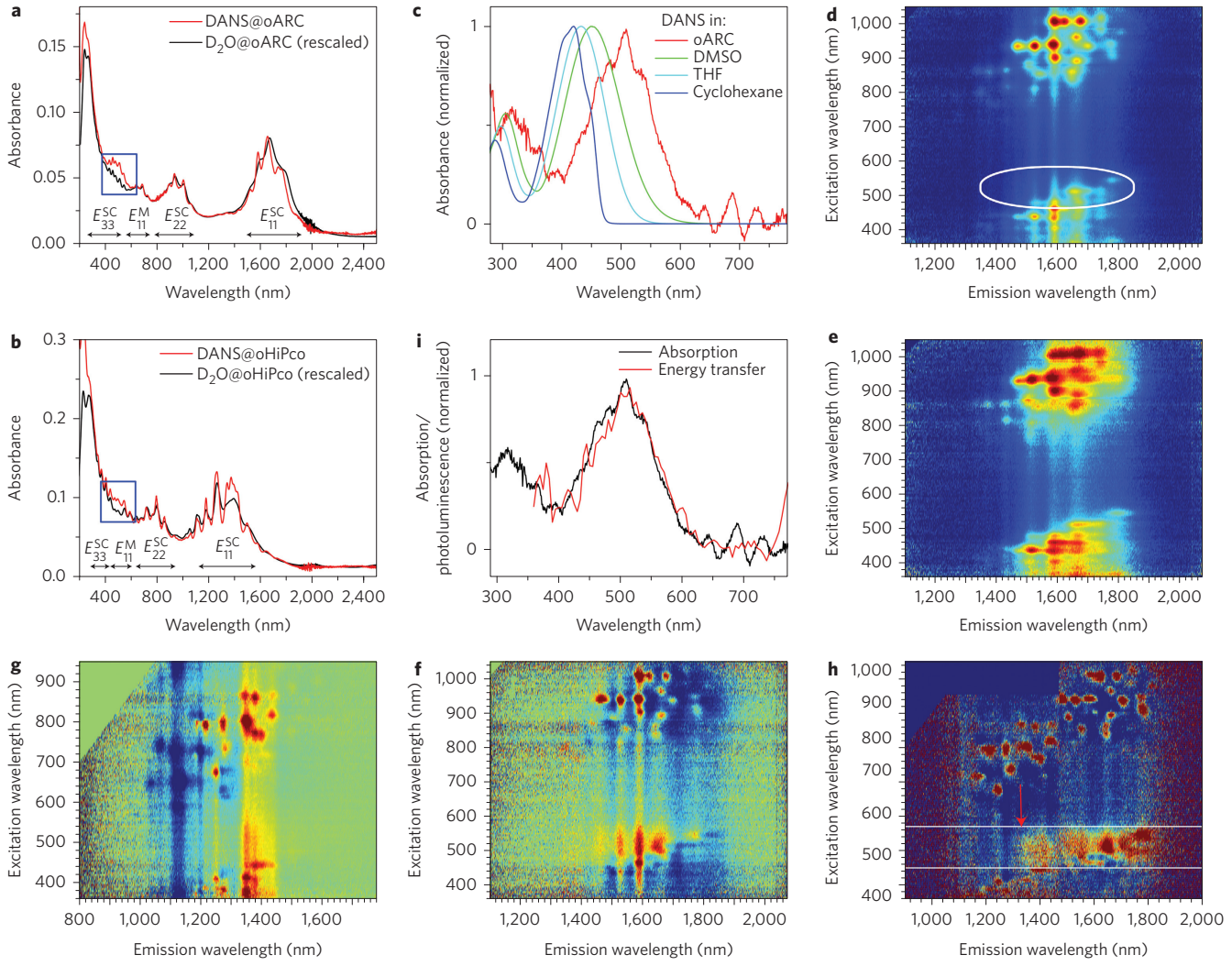

Figure 2 | Absorption and PLE spectroscopy. a,**b**, Absorption spectra of DANS@oARC and DANS@oHiPco (1 mm path length) compared to the rescaled spectrum of the D_2O@oARC and D_2O@oHiPco samples (ARC and HiPco samples are synthesized by arc discharge and high-pressure carbon monoxide methods, respectively). The different regions of the characteristic SWCNT absorption bands (due to the diameter- and chiral structure-dependent van Hove singularities in the density of states[13]) of the semiconducting (E_{ii}^{SC}) and metallic (E_{ii}^{M}) SWCNTs are indicated. In the region around 500 nm, absorption of the encapsulated DANS molecules can be observed (blue boxes), which is clearer after subtraction of the SWCNT absorption (**c**). **c**, DANS absorption band, obtained by subtracting the D_2O@oARC absorption spectrum from the DANS@oARC absorption spectrum, compared to the spectra of free DANS molecules in solvents with increasing polarity (cyclohexane, tetrahydrofuran and dimethylsulphoxide). The observed redshift for the encapsulated molecules is consistent with polar alignment (Supplementary Section 7). **d**, PLE map of DANS@oARC. The ellipse indicates the position of the energy-transfer band, which can be more clearly visualized by subtracting the pure SWCNT PLE signals (**f**). **e**, PLE map of D_2O@oARC (for other maps see Supplementary Figs 5 and 6). **f**, PLE difference map obtained by subtracting D_2O@oARC from DANS@oARC (red, positive; green, 0; blue, negative), revealing clearly the energy-transfer band located at an excitation wavelength of ~500 nm (that is, excitation in the absorption band of the DANS molecules followed by infrared emission by the SWCNTs). The imperfect subtraction of the nanotube peaks (mainly in the upper half of the panel, corresponding to excitation in E_{22}^{SC}) illustrates the shifts of the electronic transitions, resulting in residual negative peaks next to positive peaks after subtraction. **g**, PLE difference map, that is, DANS@oHiPco – D_2O@oHiPco, showing the onset of the energy-transfer band at 1,350 nm, indicative of the critical diameter for filling. However, one should be careful in concluding directly from these raw difference maps, as the energy-transfer signal here is still modulated by the abundance (and fluorescence efficiency) of the SWCNTs emitting at different wavelengths. To account for this, we also constructed difference maps after normalizing the PLE over the intensity of the intrinsic SWCNT signals (directly excited in their E_{22} transition at longer wavelengths) at the corresponding emission wavelength (**h**; Supplementary Fig. 9). **h**, Joint PLE subtraction maps for the HiPco and ARC samples, after normalization on the SWCNT E_{22} excitation, prominently showing the onset (red arrow) of the energy-transfer band (between the white lines). This clearly confirms that energy transfer only occurs for SWCNTs emitting at ~1,350 nm or longer, corresponding to a critical diameter for filling of 1.08–1.1 nm (Supplementary Figs 7–9). **i**, Comparison of the DANS absorption and the excitation profile of the energy-transfer band (that is, integral of **h** over emission wavelengths 1,300–1,700 nm).

model[22] (Supplementary Section 5b), this allows β to be extrapolated to the static (low-frequency) limit β_0, which is the more appropriate quantity to compare for different samples, as the near-resonant values are difficult to compare due to the differences in both the absorption band position and width. We obtained HRS signals from DANS@oSWCNT, which are enhanced by a factor of 54–69 (depending on the SWCNT diameter range) compared to the free DANS molecules in chloroform solution. Using equation (2) this implies effective average domain sizes of perfectly head-to-tail aligned molecules of up to ~69 molecules. This also allows us to derive the hyperpolarizabilities of the entire DANS@oSWCNT hybrid assemblies (Fig. 4 and Supplementary Section 5), which

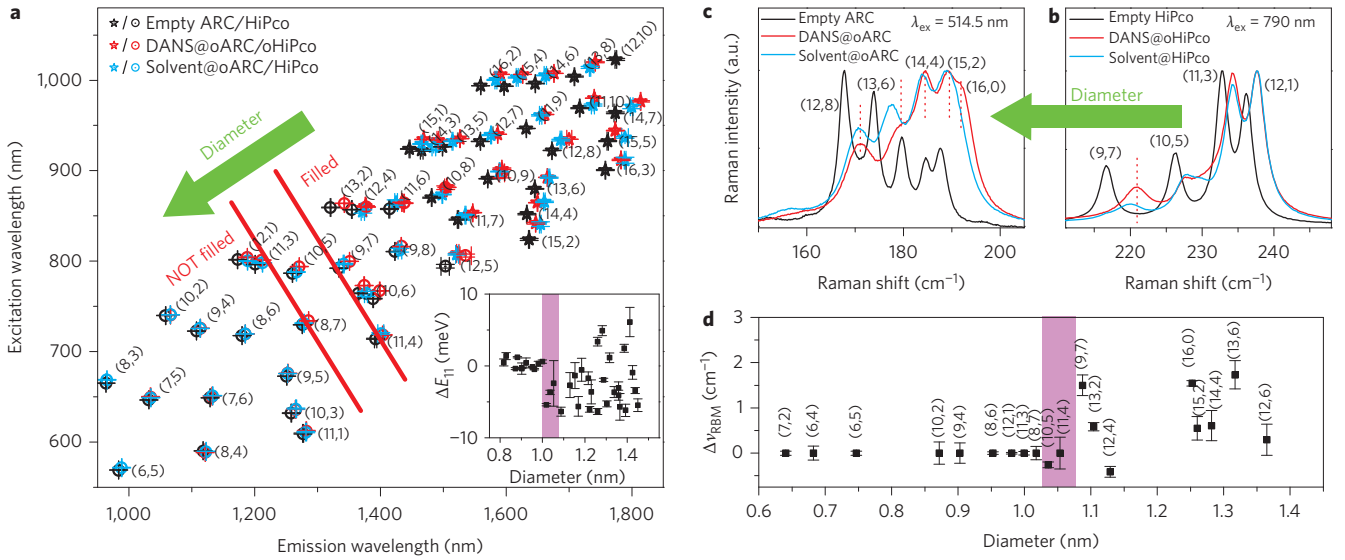

Figure 3 | Raman and PLE shifts showing the critical diameter for DANS encapsulation. a, PLE peak positions from the two-dimensional fits (Supplementary Fig. 10), showing that for small diameters no difference is observed between the solvent-filled and DANS-filled SWCNTs. Green arrow goes from higher to lower diameter tubes. Inset: Electronic shifts ($\Delta E_{11} = E_{11}^{\text{DANS@oSWCNT}} - E_{11}^{\text{solvent@oSWCNT}}$), with a clear onset starting at 1.02 nm. The intermediate region, that is, partial filling, is indicated by the coloured band. **b**,**c**, Raman spectra of empty (black), DANS-filled (red) and solvent-filled (blue) SWCNTs excited at two different wavelengths. Vertical lines indicate peak positions of DANS-filled SWCNTs. In **b**, for the slightly thinner (12,1) and (11,3) tubes, no difference is observed between the DANS@oSWCNT and solvent@oSWCNT samples, while for the (9,7) tube a clear shift can be observed, as well as for larger-diameter tubes excited at 514.5 nm (**c**). For the intermediate diameter range, only partial filling is observed ((10,5) in **b**; see Supplementary Section 4 for fits and other chiralities). **d**, Results of the Raman fits (Supplementary Figs 12–16) presenting the vibrational shifts ($\Delta\nu_{\text{RBM}} = \nu_{\text{RBM}}^{\text{DANS@oSWCNT}} - \nu_{\text{RBM}}^{\text{solvent@oSWCNT}}$) also showing the onset of encapsulation at ~1.02–1.08 nm. All error bars represent standard deviations as determined from the fitting procedure.

are the tensorial sum of the molecular hyperpolarizabilities, yielding an extremely high static value of $\beta_0 = 9{,}770 \times 10^{-30}$ e.s.u. and a peak value $\beta = 68{,}800 \times 10^{-30}$ e.s.u. (compared to $\beta_0 = 141 \times 10^{-30}$ e.s.u. and $\beta = 1{,}600 \times 10^{-30}$ e.s.u. for the free DANS molecules). The assemblies also have a huge total dipole moment, scaling with the same factor (also $\sim n$ times the molecular dipole moment, ignoring the additional enhancement of the molecular dipole moment through polarization by its neighbours), hence on the order of 500 D for the present systems. This largest enhancement factor is obtained for the thinner SWCNT samples (Fig. 4b), which ensure all DANS is included as a single molecular file, while some of the larger-diameter SWCNTs might allow for a double file (possibly antiparallel) stacking. In general, the fact that in larger-diameter SWCNTs a less-than-ideal alignment may occur implies that the actual number of perfectly aligned molecules in the thinnest SWCNTs fitting exactly one row of molecules may be even somewhat higher than the effective ensemble average observed experimentally.

To assess the degree of alignment that could be expected theoretically, we devised a simple model accounting for dipole–dipole interactions (Fig. 4c and Supplementary Section 6) and using realistic parameters based on the structure of DANS. This is essentially a one-dimensional Ising model[23] (as has also been adopted for single files of hydrogen-bonded water molecules[24]), with ferroelectric coupling between dipoles, but note that here the configuration of the dipoles is fixed at synthesis. The model yields an estimate of

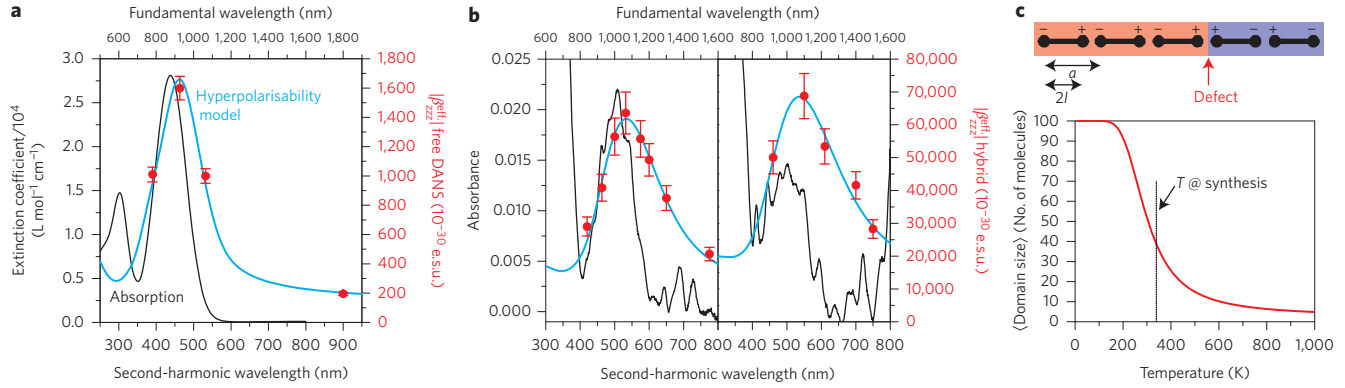

Figure 4 | Wavelength-dependent NLO polarizability. a,**b**, β (red) compared with DANS absorption spectra (black; 1 cm path length) and fitted with the β dispersion models (blue) for the free DANS molecules in chloroform solution (**a**) and the DANS@oARC (**b**, left) and DANS@oHiPco (**b**, right) hybrid assemblies. Error bars (5% in **a**, 10% in **b**) represent a conservative estimate of the standard deviation from multiple measurements. **c**, Theoretical simulation of the degree of alignment for a one-dimensional array of 100 molecules with a dipole moment of 9.14 D each, using the shown schematic model (top: depicted with a defect separating two ordered domains shown as red and blue areas), with realistic parameters for DANS obtained from semi-empirical calculations at the Hartree–Fock level ($a = 16.88$ Å, $2l = 12.17$ Å, see main text and Supplementary Section 6).

the expected HRS enhancement factor of ~42 molecules, on the same order of magnitude as the experimental results. This high degree of order is remarkable considering that Ising already pointed out that no phase transitions can occur in a one-dimensional system with short-range (dipole–dipole) interactions[23]. Moreover, as the average domain size is determined by the Boltzmann statistics of defect formation and thus depends exponentially on the dipole–dipole interaction energy divided by k_BT, slight modifications to the molecular dipole moment or to the exact spacing, as well as to the temperature used during synthesis, can easily improve the degree of alignment by another order of magnitude or more.

In summary, asymmetric molecules can be inserted into SWCNTs with a diameter above a well-defined critical value, yielding head-to-tail aligned arrays with extremely large hyperpolarizabilities. Moreover, these dye-filled SWCNTs form chemically inert building blocks that are solution-processible as individual entities (in contrast to inclusion in zeolites[25,26]); their huge total dipole moment and size promise good and stable alignment in electric fields. Thus, this unusual polar order achievable inside carbon nanotubes is a useful approach towards the rational design of solution-processible yet stable NLO materials. We also note this concept can be readily extended to other directional properties.

Methods

To cover the appropriate range of diameters d to fit a typical dipolar NLO molecule (such as DANS[4]), SWCNTs produced by the arc discharge method[5] (ARC; d = 1–1.5 nm) and by the high-pressure carbon monoxide method[27] (HiPco; d = 0.7–1.2 nm) were used. Details of the encapsulation procedure are provided in Supplementary Section 1. In brief, the SWCNTs were first chemically treated to open the nanotube ends (resulting in opened SWCNT samples denoted oARC and oHiPco). The Raman spectra of these opened SWCNTs (Supplementary Fig. 17) hardly show a D-band (defect-induced band[6]), demonstrating a negligible number of defects in the SWCNT walls. The high quality of the oSWCNTs was further confirmed by the narrow RBM line widths and the occurrence of significant photoluminescence (Supplementary Section 3). The encapsulation was then performed by refluxing the opened nanotubes in a saturated solution of DANS in tetrahydrofuran. The excess DANS molecules were removed by repeated rinsing and filtration with dichloromethane, and the resulting filled SWCNTs (DANS@oSWCNT) were solubilized in D_2O with sodium deoxycholate (DOC) as surfactant[28] and further purified by density gradient ultracentrifugation[16,29], thus separating the individually solubilized SWCNTs from any SWCNT bundles and other impurities based on their different densities (Supplementary Fig. 1). For spectroscopic characterization of the DANS encapsulation, various reference samples were also prepared (Supplementary Table 1), for example by following the same procedure but without opening the SWCNTs or without adding DANS (solvent@oSWCNT). Extensive characterization data and details of the methodology are provided in Supplementary Sections 2–5.

Received 15 February 2014; accepted 6 January 2015; published online 2 February 2015

References

1. Tao, N. J. Electron transport in molecular junctions. *Nature Nanotech.* **1,** 173–181 (2006).
2. Dalton, L. R., Sullivan, P. A. & Bale, D. H. Electric field poled organic electro-optic materials: state of the art and future prospects. *Chem. Rev.* **110,** 25–55 (2009).
3. Cho, M. J. *et al.* Recent progress in second-order nonlinear optical polymers and dendrimers. *Prog. Polym. Sci.* **33,** 1013–1058 (2008).
4. Oudar, J. L. Optical nonlinearities of conjugated molecules. Stilbene derivatives and highly polar aromatic compounds. *J. Chem. Phys.* **67,** 446–457 (1977).
5. Iijima, S. Helical microtubules of graphitic carbon. *Nature* **354,** 56–58 (1991).
6. Dresselhaus, M. S., Dresselhaus, G. & Avouris, P. in *Topics in Applied Physics* Vol. 80 (2001).
7. Takenobu, T. *et al.* Stable and controlled amphoteric doping by encapsulation of organic molecules inside carbon nanotubes. *Nature Mater.* **2,** 683–688 (2003).
8. Yanagi, K., Miyata, Y. & Kataura, H. Highly stabilized β-carotene in carbon nanotubes. *Adv. Mater.* **18,** 437–441 (2006).
9. Gaufrès, E. *et al.* Giant Raman scattering from J-aggregated dyes inside carbon nanotubes for multispectral imaging. *Nature Photon.* **8,** 72–78 (2014).
10. Marder, S. R., Perry, J. W. & Schaefer, W. P. Synthesis of organic salts with large second-order optical nonlinearities. *Science* **245,** 626–628 (1989).
11. Yi, T. *et al.* J-aggregated dye–$MnPS_3$ hybrid nanoparticles with giant quadratic optical nonlinearity. *Adv. Mater.* **17,** 335–338 (2005).
12. Singer, K. D., Sohn, J. E. & Lalama, S. J. Second harmonic generation in poled polymer films. *Appl. Phys. Lett.* **49,** 248–250 (1986).
13. Bachilo, S. M. *et al.* Structure-assigned optical spectra of single-walled carbon nanotubes. *Science* **298,** 2361–2366 (2002).
14. Shin, D. M. & Whitten, D. G. Solvatochromic behavior of intramolecular charge-transfer diphenylpolyenes in homogeneous solution and microheterogeneous media. *J. Phys. Chem.* **92,** 2945–2956 (1988).
15. Wenseleers, W. *et al.* Effect of water filling on the electronic and vibrational resonances of carbon nanotubes: Characterizing tube opening by Raman spectroscopy. *Adv. Mater.* **19,** 2274–2278 (2007).
16. Cambré, S. & Wenseleers, W. Separation and diameter-sorting of empty (end-capped) and water-filled (open) carbon nanotubes by density gradient ultracentrifugation. *Angew. Chem. Int. Ed.* **50,** 2764–2768 (2011).
17. Cambré, S. *et al.* Experimental observation of single-file water filling of thin single-wall carbon nanotubes down to chiral index (5,3). *Phys. Rev. Lett.* **104,** 207401 (2010).
18. Cambré, S. *et al.* Luminescence properties of individual empty and water-filled single-walled carbon nanotubes. *ACS Nano* **6,** 2649–2655 (2012).
19. Terhune, R. W., Maker, P. D. & Savage, C. M. Measurements of nonlinear light scattering. *Phys. Rev. Lett.* **14,** 681–684 (1965).
20. Campo, J., Desmet, F., Wenseleers, W. & Goovaerts, E. Highly sensitive setup for tunable wavelength hyper-Rayleigh scattering with parallel detection and calibration data for various solvents. *Opt. Express* **17,** 4587–4604 (2009).
21. Guo, G. Y., Chu, K. C., Wang, D-S. & Duan, C-G. Linear and nonlinear optical properties of carbon nanotubes from first-principles calculations. *Phys. Rev. B* **69,** 205416 (2004).
22. Campo, J. *et al.* Practical model for first hyperpolarizability dispersion accounting for both homogeneous and inhomogeneous broadening effects. *J. Phys. Chem. Lett.* **3,** 2248–2252 (2012).
23. Ising, E. Beitrag zur theorie des ferromagnetismus. *Zeitschrift für Physik* **31,** 253–258 (1925).
24. Köfinger, J. & Dellago, C. Single-file water as a one-dimensional Ising model. *New J. Phys.* **12,** 093044 (2010).
25. Cox, S. D., Gier, T. E., Stucky, G. D. & Bierlein, J. Inclusion tuning of nonlinear optical materials: switching the SHG of *p*-nitroaniline and 2-methyl-*p*-nitroaniline with molecular sieve hosts. *J. Am. Chem. Soc.* **110,** 2986–2987 (1988).
26. Pham, T. C. T., Kim, H. S. & Yoon, K. B. Large increase in the second-order nonlinear optical activity of a hemicyanine-incorporating zeolite film. *Angew. Chem. Int. Ed.* **52,** 5539–5543 (2013).
27. Bronikowski, M. J. *et al.* Gas-phase production of carbon single-walled nanotubes from carbon monoxide via the HiPco process: a parametric study. *J. Vac. Sci. Technol. A* **19,** 1800–1805 (2001).
28. Wenseleers, W. *et al.* Efficient isolation and solubilization of pristine single-walled nanotubes in bile salt micelles. *Adv. Funct. Mater.* **14,** 1105–1112 (2004).
29. Arnold, M. S. *et al.* Sorting carbon nanotubes by electronic structure using density differentiation. *Nature Nanotech.* **1,** 60–65 (2006).
30. Dewar, M. J. S., Zoebisch, E. G., Healy, E. F. & Stewart, J. J. P. Development and use of quantum mechanical molecular models. 76. AM1: a new general purpose quantum mechanical molecular model. *J. Am. Chem. Soc.* **107,** 3902–3909 (1985).

Acknowledgements

The authors thank W. Van Werveke for preliminary work indicating a similar alignment with a different NLO chromophore (Disperse Red 1). Financial support from the Fund for Scientific Research – Flanders (FWO) for the SWCNT work (projects G040011N, G021112N and 1513513N) and for the NLO measurements (projects G.0129.07, G.0206.12, 1523913N and G.0522.13N) is acknowledged. Part of this work was supported by a UA-NOI-BOF grant, the Hercules Foundation, and EU ITN Nano2Fun. S.C. and J.C. are postdoctoral fellows of the FWO.

Author contributions

S.C. performed most of the synthesis and designed and performed most Raman and PLE experiments. J.C. designed and performed the HRS experiments and some synthesis. C.B. conducted part of the initial synthesis and spectroscopic characterization of DANS@oARC samples. C.V. independently reproduced the synthesis for the HiPco samples and part of the spectroscopic characterization. P.C. performed the thermogravimetric analysis. W.W. conceived the idea and co-designed and supervised all experiments. All authors contributed to writing the manuscript.

Additional information

Supplementary information is available in the online version of the paper. Reprints and permissions information is available online at www.nature.com/reprints. Correspondence and requests for materials should be addressed to W.W.

Competing financial interests

The authors declare no competing financial interests.

nature nanotechnology

SUPPLEMENTARY INFORMATION

DOI: 10.1038/NNANO.2015.1

Asymmetric dyes align inside carbon nanotubes to yield a large nonlinear optical response

Sofie Cambré , Jochen Campo, Charlie Beirnaert, Christof Verlackt, Pegie Cool, and Wim Wenseleers

Table of Contents

S1. Materials

a. Opening of the SWCNTs

Raw (closed) arc-discharge SWCNTs (ARC) were obtained from Nanoledge (batch P00508D) and opened by air oxidation and acid treatment. This procedure has previously been shown to be 100% efficient in opening the SWCNTs for filling with other molecules[1,2]. In brief, the SWCNTs were heated in air at 365ºC, up to a total weight loss of 50%, to remove other carbonaceous material present in the raw SWCNT sample. In a second step, the SWCNTs were treated ultrasonically (bath sonicator: Bransonic, 1510E-MTH, 70W, 42kHz) in concentrated (37%) HCl at 60ºC, to remove the catalytic nanoparticles and open the SWCNTs. Afterwards, the SWCNTs were neutralized by excessive rinsing with deionised water and vacuum filtration (5µm polycarbonate filter, Whatman). Finally, the so-obtained powder was annealed at 800ºC for 1 hour in vacuum to remove any residual functional groups which can block the SWCNT-ends. We will further denote these opened SWCNTs as oARC.

Purified high-pressure CO conversion SWCNTs (HiPco) were obtained from Carbon Nanotechnologies Inc. (batch P0279). These tubes are already partially opened and water molecules, as well as solvent molecules (i.e. tetrahydrofuran (THF) or dichloromethane (DCM) used in the encapsulation procedure (see section S1.b)) can be encapsulated. Filling with the larger DANS molecules however required an additional opening procedure (most probably functional groups on the SWCNT-ends prevent the DANS encapsulation). Complete opening was achieved by applying the same procedure as for the ARC tubes but using an oxidation temperature of 375ºC (determined based on thermogravimetric analysis of the raw sample), resulting in the oHiPco sample.

b. Encapsulation procedure

The encapsulation procedure is based on the work of Yanagi *et al.*[3,4]. Opened SWCNTs (15mg) were dispersed in a saturated solution of DANS (50 mg, 4-dimethylamino-4′-nitrostilbene, Sigma, ≥99.8%) in THF (15mL, solubility DANS in THF=3.2mg/mL) and refluxed for 15 hours under nitrogen atmosphere. THF was chosen as a solvent with moderate solubility and optimal stability for the DANS molecules. Non-encapsulated DANS molecules were removed by washing with DCM (~150mL, 3-4 washing cycles), in which DANS is more soluble, using a vacuum filtration setup with a PTFE membrane (0.5µm pore size). The so-obtained powder samples were subsequently dried in air for 3 days at room temperature before solubilisation, yielding DANS@oARC and DANS@oHiPco (~15-16.2mg). The overall yield is close to quantitative, with a maximum loss of SWCNTs of <~5% (e.g. sticking to the glassware and filter membrane).

To allow for characterisation by thermogravimetric (TGA) and elemental analysis, the encapsulation procedure was repeated on a larger scale (~50-80mg SWCNTs) with commercially purified (and, as a side effect, opened – as verified by high resolution Raman spectroscopy[1,5]) SWCNTs, namely plasma torch SWCNTs (oPLT) from Raymor Nanotech (RN-220, Lot#RNL14-220-219) and arc-discharge SWCNTs (oARC2) from Carbon Solutions Inc. (P2-SWCNT, batch#02-153). The oPLT sample has an identical diameter distribution as the oARC sample (as determined by optical absorption spectroscopy; with ~1.4nm average diameter), while the oARC2 sample has slightly larger average diameter (d_{av}~1.5nm). Both SWCNT samples were first annealed in high vacuum up to 800ºC to remove any residual functionalization[6]. The

encapsulation was verified with optical spectroscopy. Optical absorption spectra show that not only the diameter distribution, but also the ratio of DANS absorption to SWCNT absorption is identical (within a few percent) for DANS@oPLT and DANS@oARC. The powder samples (DANS@oPLT and DANS@OARC2) were analysed using thermogravimetric (TGA) and elemental analysis (see section S1.f).

c. Solubilization procedure

The DANS@oSWCNT samples (10mg) were solubilised in a 1% DOC/D_2O solution (3mL), using a combination of bath sonication (1 hour) followed by magnetic stirring for several weeks in order to get a high amount of DANS@oSWCNT individualized in solution. D_2O is used for its increased optical transparency in the infrared compared to H_2O.

The solutions were centrifuged at 16215g (14000rpm; Sigma 2-16KCH centrifuge with swing-out rotor) to remove large bundles and undissolved material. For DANS@oSWCNT, the centrifugation time was limited to 1 hour, in order not to lose too many DANS-filled SWCNTs in this pre-centrifugation step, while for most SWCNT reference samples a 24 hours pre-centrifugation was applied. In a second step, the solutions were further purified (i.e. to remove bundles, essential for the spectroscopic characterization) using density gradient ultracentrifugation (DGU, see section S1.e).

d. Reference samples

Several reference samples were prepared to ultimately prove the encapsulation of the DANS molecules and distinguish it from adsorption on the outer walls, or from encapsulation of solvent molecules that are used in the preparation procedure (i.e. D_2O, THF and DCM).

As a first set of reference samples, the opened SWCNTs were solubilised without exposing them to THF or DCM, thus resulting in water-filled SWCNTs[1,5]: samples D_2O@oARC and D_2O@oHiPco. Secondly, by following the entire encapsulation procedure without adding the DANS-molecules to the solution, the opened SWCNTs can get filled with the solvents: solvent@oARC and solvent@HiPco. The encapsulation procedure was furthermore applied using closed SWCNTs, in which the DANS-molecules cannot be encapsulated. For this purpose we used the raw ARC and HiPco tubes: DANS/ARC and DANS/HiPco. Note that the as-received HiPco sample was found to be partially opened already, as evidenced by the solvent filling (resulting in RRS peak shifts which are identical for solvent@oARC and solvent@HiPco in the overlapping diameter range, but different from those of the water-filled samples), but not sufficiently so to yield efficient filling with DANS, indicating that functional groups at the tube ends (remaining from the acid treatment used during purification) were blocking the entrance to the larger DANS molecules. Therefore the opening procedure and annealing as described in section S1.a was performed for both SWCNT types before filling with DANS: DANS@oARC and DANS@oHiPco. Finally, also a reference sample with closed and thus empty SWCNTs was prepared as described in ref. [7], using a carefully solubilised SWCNT sample and isolating the empty tubes by DGU: empty ARC and empty HiPco.

Table S1. Short description of the different samples studied in this work.

Sample names	**Description**
D_2O@oARC and D_2O@oHiPco	opened SWCNTs filled with D_2O
solvent@oARC	opened ARC SWCNTs filled with a combination of THF, DCM and/or D_2O
solvent@HiPco	HiPco SWCNTs filled with a combination of THF, DCM and/or D_2O (these commercial HiPco tubes were found to be opened sufficiently to encapsulate the solvents)
DANS/HiPco	HiPco SWCNTs refluxed in a saturated THF solution of DANS, washed with DCM and solubilised in D_2O (these commercial SWCNTs were found to be insufficiently opened for DANS encapsulation)
DANS/ARC	closed ARC SWCNTs refluxed in a saturated THF solution of DANS, washed with DCM and solubilised in D_2O
DANS@oARC and DANS@oHiPco	DANS molecules encapsulated in the opened SWCNTs
empty ARC and empty HiPco	empty (closed) SWCNTs
DANS@oARC2	DANS molecules encapsulated in industrially opened arc-discharge SWCNTs (d_{av} ~ 1.5nm): large batch for TGA and elemental analysis
DANS@oPLT	DANS molecules encapsulated in industrially opened Plasma Torch SWCNTs (identical diameter range as oARC, d_{av} ~ 1.4nm): large batch for TGA and elemental analysis

e. Density gradient ultracentrifugation (DGU)

After solubilisation and pre-centrifugation at 16215g, DGU was performed to remove all bundles from the solution, essential for the spectroscopic characterization of the DANS-filled SWCNTs. Thus, we collected the entire band of individualized SWCNTs from the centrifuge tubes (as opposed to performing any chirality/diameter sorting, for which DGU is mostly known[8]), as here the purpose was only to achieve a very thorough removal of bundles – more thoroughly and more efficiently so than possible by the usual, rate based separations without gradient medium. The density gradient medium, iohexol (5-(N-2,3-dihydroxypropylacetamido)-2,4,6-triiodo-N,N'-bis(2,3-dihydroxypropyl)isophthalamide, tradename "NycoDenz"), was obtained from Axis-Shield in powder form, and dissolved in D_2O at appropriate concentrations to obtain the desired density ranges, as detailed below. Gradients were prepared, in a similar way as described in ref. [7], in 1.3mL polyallomer centrifuge tubes. A low density layer (ρ=1.20g/mL, 0.7mL), including the SWCNTs, was superimposed on top of a high density layer (ρ=1.265g/mL, 0.6mL). A quasi-linear gradient was achieved by tilting the centrifuge tube and rotating it around its long axis to mix the two layers. The surfactant concentration was kept constant throughout the layers at

0.7%w/v DOC in D_2O, which we found to be very efficient in separating the individual SWCNTs from the bundles. Ultracentrifugation at 122000g for 48 hours (until equilibrium) then allows for isolating the individualized DANS@oSWCNTs, which possess a density of 1.21-1.22g/mL. In comparison, the density of DANS-crystals dispersed in a 1%w/v DOC/D_2O solution (in which DANS is completely insoluble) was determined to be 1.32g/mL and also the bundles are much denser than the individualized (DANS-filled) SWCNTs (≥ ~1.3g/mL), hence ending up close to the bottom of the centrifuge tube. The empty, closed SWCNTs can be found at a density of 1.16-1.19g/mL. Figure S1 shows a typical photograph of the centrifuge tubes after DGU-centrifugation.

For the absorption experiments, part of the solutions after DGU were dialyzed (10KDalton MWCO dialysis cassettes) in 1%DOC/D_2O solution for removal of the gradient medium, which absorbs strongly below 300 nm.

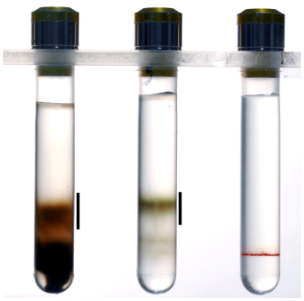

Figure S1. Photograph of the centrifuge tubes after DGU. Left: a DANS@oARC sample, center: a D_2O@oARC sample, right: DANS-crystals dispersed in DOC/D_2O. Since the D_2O@oARC sample was pre-centrifuged for 24h, no bundles are visible in the centrifuge tube, while for the DANS@oARC (only 1h pre-centrifugation) the bottom of the centrifuge tube is filled with bundles. The black bars indicate the fractions that were collected for the experiments, containing the individualized DANS@oSWCNTs and D_2O@oSWCNTs. For comparison, also the DANS-crystals dispersed in DOC/D_2O are shown, that have a much larger density than the individualized DANS-filled SWCNTs. The DANS@oARC sample clearly has a more reddish colour than the D_2O@oARC SWCNTs, giving a first hint of the DANS-encapsulation.

f. Thermogravimetric and elemental analysis

In the wavelength-dependent RRS data (see also section S4), the relative amplitudes of the RBM-peaks of empty, water- or solvent-filled and DANS-filled SWCNTs (Figures S12-S16) give detailed information (for each chirality separately) on the fraction of SWCNTs that is filled with DANS, which is close to 100% for most chiralities (96% on average for diameters ≥1.1nm or ~91% for the DANS@oARC sample as a whole ; see section S4) – however, it does not provide the density of DANS molecules in these filled (sections of) SWCNTs. In contrast, thermogravimetric (TGA) and elemental analysis provide the mass-fraction of DANS molecules with respect to SWCNTs, thus yielding complementary information on the filling efficiency.

For the theoretical model of a completely filled (9,7) SWCNT as shown in Figure 1d this mass fraction is 10.14% (with very small uncertainty, <~0.3%, as sterical hindrance excludes significant variation in molecular orientation). For smaller diameters, the DANS molecules cannot be encapsulated. For larger diameters, this maximum mass fraction is expected to reduce initially (inversely proportional to *d*), as long as only a single molecular file enters the SWCNT (potentially reducing the mass fraction down to ~7.88-7.35% for 1.4-1.5nm thick SWCNTs). However, for the larger SWCNTs among the ARC and PLT materials, significant tilt and overlap

of subsequent molecules in the array might occur, potentially compensating for this reduction, such that for the very largest SWCNTs present among the ARC and PLT materials, the theoretical mass percentage of DANS for 100% filled tubes may be anywhere between ~6-10%.

Thermogravimetric analysis (TGA) was performed on a Mettler Toledo TGA/SDTA851e thermobalance. Samples were heated from room temperature up to 800°C at a rate of 1°C/min under O_2 flow. Figure S2 presents the TGA and derivative TGA (DTGA) curves of the DANS@oPLT and DANS@oARC2 samples, in comparison with the pure DANS powder and the annealed oARC2 and oPLT powder samples. The pure DANS molecules decompose in two well-resolved steps, of which the first component corresponds to 32.16% of the total DANS mass. The TGA curves of the oPLT and oARC2 materials show that at high temperature about 27.5% resp. 13.5% of non-combustible material, i.e. the catalyst particles (as metallic particles and/or their oxides), remains (the slight increase in weight of the oPLT material above 640ºC, to

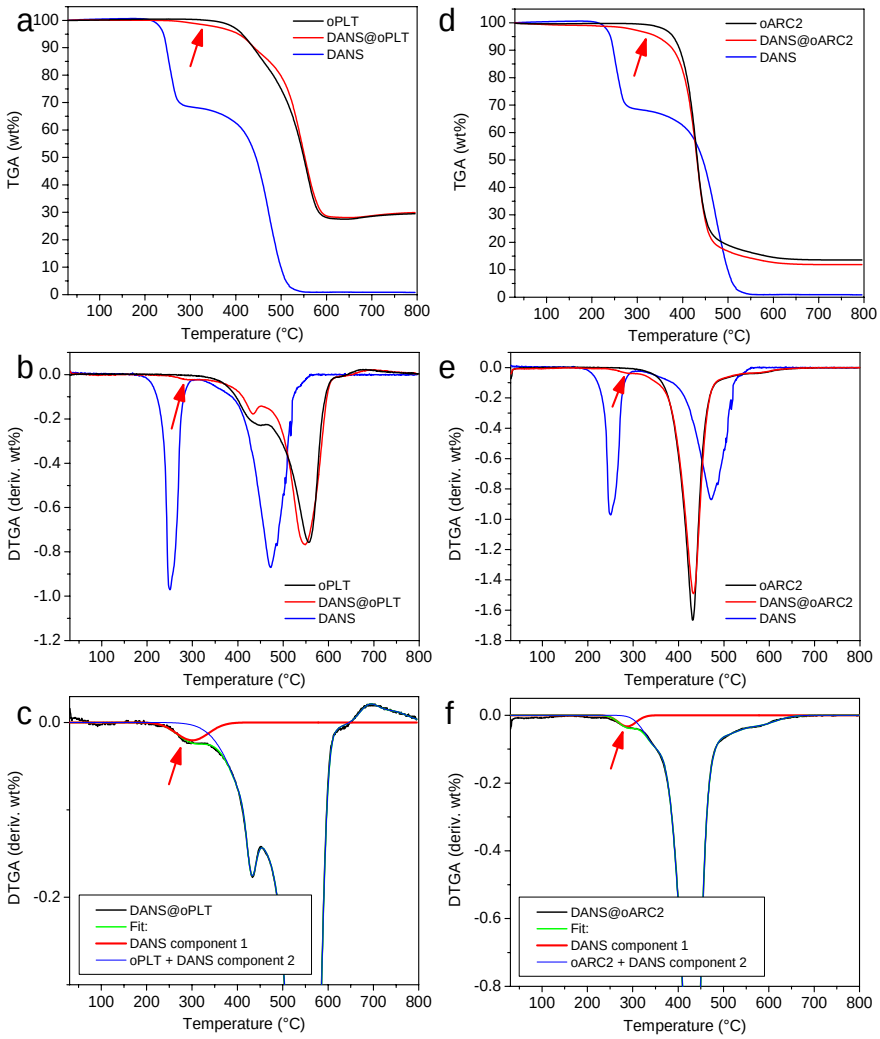

Figure S2. TGA analysis of the filling efficiency. a,d) TGA for the pure DANS powder (blue), the annealed SWCNTs (black) and DANS@oSWCNT (red), **b,e**) DTGA of each of these samples and **c,f**) Experimental curve (black) and multi-Gaussian fit (green) of the DTGA curve of DANS@oSWCNT (black), consisting of one Gaussian for the first component of DANS (red) and several for the other organic material (oSWCNT + second component of DANS, blue). The red arrow in each of the panels indicates the first decomposition component of the DANS molecules when encapsulated in the SWCNTs.

~30% at 800ºC, is attributed to further oxidation of the Ni Fe Co catalyst). The non-carbonaceous material is not considered in the further analysis to assess the filling efficiency, i.e. mass fractions refer to fractions of the total combustible (organic) content (which consists largely of SWCNTs, as the purification of SWCNT samples removes most non-SWCNT carbonaceous material, at least for ARC2). Mass fractions of different decomposition components are derived based on multi-Gaussian fits of the DTGA curves.

For the DANS@oSWCNT samples, the first decomposition component of DANS can be clearly distinguished in the DTGA curves, as an additional contribution compared to the DTGA of the pure oSWCNT samples, and is shifted to higher temperature (from 251ºC to 296ºC), nicely illustrating that the organic chromophores are strongly protected by the (encapsulation in the) SWCNTs. Since the other component overlaps completely with the decomposition of the SWCNTs, the total DANS mass can be more accurately evaluated based on the first component only, assuming the ratio of both decomposition steps is the same as for the pure DANS compound. This yields total DANS mass fractions of 7.6% for DANS@oPLT and 6.0% for DANS@oARC2, within the theoretical range expected for completely filled SWCNTs.

Because of the non-negligible uncertainties associated with the analysis of the TGA measurements, we also obtained more specific information on the sample composition by elemental analysis of these samples (ALS Environmental, Tucson Arizona). Results are presented in Table S2. The mass-percentage of DANS in the DANS@oSWCNT samples was derived by fitting the elemental compositions to a linear combination of the experimental composition of the corresponding pure oSWCNT material, and the formula composition of DANS. The most precise measure of DANS concentration is provided by the percentages of N and H only, which are not present to a significant extent in the SWCNT materials themselves, as opposed to carbon, as well as oxygen which moreover can be either taken up or released by the partly oxidised catalyst particles. Therefore, we only considered the H and N contributions in the fit. As such we obtain a mass percentage of DANS of 5.4% in DANS@oPLT and 6.8% in DANS@oARC2. The uncertainty on these percentages is estimated to be <~0.5%, based on the agreement with the other elements. Within the theoretical model of a perfect one-dimensional (1D) chain of molecules, and average-diameters of both SWCNT samples, this corresponds to ~69% of the SWCNTs being filled for DANS@oPLT and ~93% for DANS@oARC2. The lower percentage obtained for the DANS@oPLT may in fact be influenced by the much lower purity of the oPLT material (containing a significant fraction of carbonaceous impurities). Thus, even though uncertainties vary in the 5-30% range, all data from RRS, TGA, and elemental analysis show that the large majority of SWCNTs are filled with DANS.

Table S2. Results and fits of the elemental analysis for DANS@oSWCNT compared to oSWCNT. The oARC2 results are an average of two separate measurements. The mass percentage of DANS is determined from a best fit of the H and N percentages, as described in the text.

Element	DANS@oPLT	oPLT	Fit (5.4% DANS)	DANS@oARC2	oARC2	Fit (6.8% DANS)
C	76.35	77.77	77.44	87.02	87.18	87.19
H	0.45	0.05	0.37	0.83	0.35	0.74
N	0.57	0.07	0.63	1.22	0.58	1.26
O	1.42	1.14	1.72	2.03	1.12	1.88

S2. Absorption spectroscopy

UV-VIS NIR absorption spectra were collected with a Varian Cary5E spectrophotometer in the range of 200-2500nm, using fused silica optical cells with different path lengths (where indicated, spectra are scaled to a common 1mm path length).

Figure S3 presents the absorption spectra of the solutions before DGU (i.e. after 16215g pre-

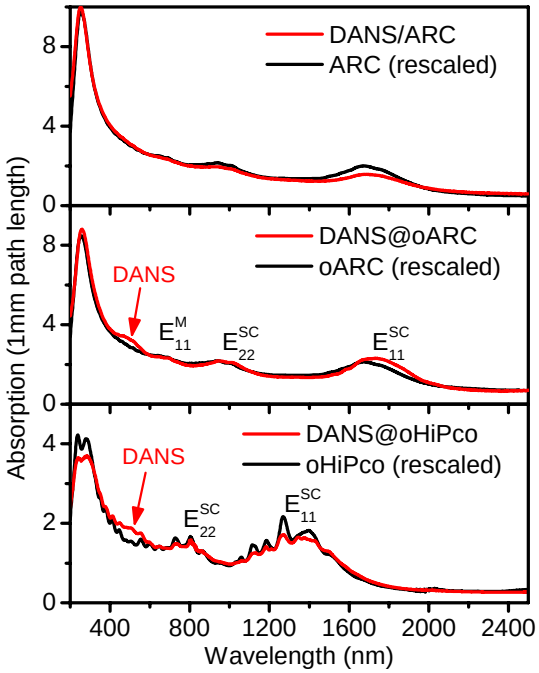

Figure S3. Absorption spectra acquired before DGU. For the opened SWCNTs (oARC and oHiPco), the absorption band of DANS (at around 500nm) is clearly distinguishable, while it is absent for the samples prepared with the closed SWCNTs. The different regions of the van Hove singularities of the semiconducting (E_{ii}^{SC}) and of the metallic (E_{ii}^{M}) SWCNTs are indicated.

centrifugation only). For DANS@oARC and DANS@oHiPco the additional absorption band due to the encapsulated DANS-molecules can be clearly observed, while it is absent for the closed SWCNTs (DANS/ARC). The washing procedure thus fully removes the excess of DANS molecules, while retaining the encapsulated ones.

After DGU, the resolution of the absorption bands increases (i.e. no bundles present, as confirmed by Raman spectroscopy) and the shifts of the electronic transitions become clear (Fig. 2). Figure S4 compares the absorption spectra of DANS@oSWCNT with those of the empty SWCNT and solvent@oSWCNT samples. The electronic transitions of the DANS-filled SWCNTs are clearly red-shifted in comparison with the empty tubes, and, more importantly, for the larger diameter tubes (i.e. longer wavelengths), this red-shift for the DANS@oSWCNT samples is significantly less than for the D_2O@oSWCNT and solvent@oSWCNT samples (i.e. a clear blue-shift is observed for the DANS@oSWCNT samples with respect to D_2O@oSWCNT and solvent@oSWCNT samples).

Besides providing a qualitative indication of the presence of the dye, the dye absorption band can also be used to determine the absolute concentration of dye molecules in the sample solutions, as

used in the analysis of the NLO data (see section S5), because the extinction coefficient of DANS is accurately known from literature, and is known to be almost independent of the molecular environment: the extinction coefficient of DANS has been shown to vary by as little as 8.7% (standard deviation) over a very wide range of solvent polarities[9], where moreover the largest deviations occurred in solvents showing solubility problems, and hence are likely just experimental errors rather than actual variations in extinction. In addition, it is in principle also possible to use the absorption data as an independent (albeit much less accurate) cross-check of the relative concentration of DANS to SWCNTs (also available from TGA and elemental analysis), or alternatively, of the relative extinction coefficients of DANS and SWCNTs. The accuracy of this cross-check is however limited by the accuracy of the TGA and elemental analysis determination of the DANS mass fraction, and, more importantly, of the extinction coefficient of SWCNTs, for which unfortunately no well-established data are available in literature to date (values varying by ~ an order of magnitude)[10,11]. A lower limit to the SWCNT oscillator strength (because based on a direct measurement, but assuming a complete solubilisation of a small, known mass of SWCNTs) is ~ 0.00125 per C atom for the E_{11} transition of semiconducting arc-discharge tubes[10]. A probably more accurate estimate is provided by the less direct, but very elaborate work in ref. [11] for a number of specific, thin SWCNTs. Scaling their result for the thickest SWCNT they considered ((9,7) SWCNT) to the diameter of ~1.3nm of our Arc samples (using an inverse proportionality with diameter[12,13]), yields oscillator strengths of 0.0035 and 0.0031 for the E_{11} and E_{22} transitions respectively. With these oscillator strengths, the integrated SWCNT absorption bands can be converted to the SWCNT concentrations, and combining this with the mass ratio of DANS to SWCNTs of ~(6.5±1)% from TGA and elemental analysis, then yields another (less accurate) estimate of the DANS concentration, and hence a rough double-check of its extinction coefficient: 13200 or 41900 L mol^{-1} cm^{-1}, when the SWCNT oscillator strength from ref. [10] or from ref. [11] is used, respectively. While obviously much less accurate than directly using the known extinction coefficient of DANS (~(28500±600) L mol^{-1} cm^{-1})[9], this cross-check shows that the experimental results are internally consistent, and can in fact be considered as a confirmation of the literature estimates of the SWCNT absorption cross-sections.

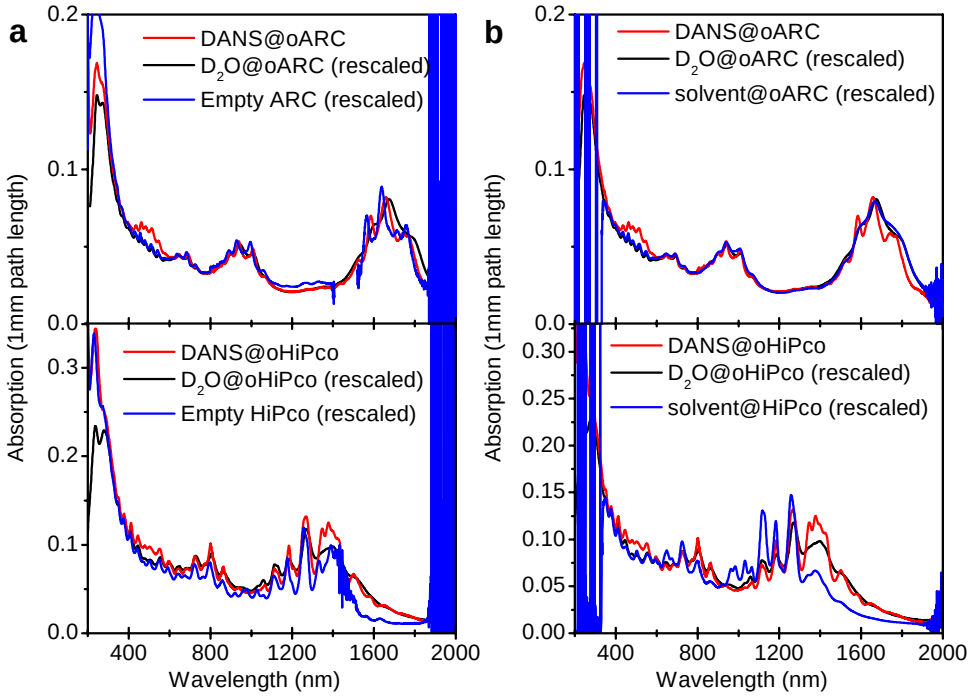

Figure S4. Absorption spectra after DGU. a, Comparison of the DANS@oSWCNT absorption spectra with empty SWCNTs and water-filled SWCNTs (the empty tubes were dialyzed in H_2O instead of D_2O, and therefore show high absorption above 1850nm, and around 1400-1500nm). **b**, Comparison of the DANS@oSWCNT absorption spectra with those of D_2O@oSWCNT and solvent@oSWCNT (the solvent@oSWCNT samples were not dialyzed and therefore show high absorption below 350nm due to the gradient medium).

S3. Photoluminescence-excitation spectroscopy (PLE)

a. Experimental details

Two-dimensional (2D) IR band-gap PLE spectra were recorded using a home-built dedicated set-up: The sample was excited with a pulsed Xe-lamp (Edinburgh Instruments, Xe900-xP920), and excitation wavelengths were spectrally selected with a 300mm grating monochromator (Acton SpectraPro 2355). Emission was collected at 90° and analyzed using a 150mm grating spectrograph (Acton SpectraPro 2156) with a liquid nitrogen cooled extended InGaAs photodiode array detector (Princeton Instruments OMA V:1024/LN-2.2), sensitive up to 2.2µm. Spectra were recorded with 5nm steps in excitation wavelength and an instrumental resolution of 8nm in excitation and 10nm in emission wavelength. Appropriate filters were used to eliminate stray light and higher order diffractions from the spectrometers, and all spectra were corrected for detector and spectrograph efficiency, filter transmission, and (temporal and spectral) variations of the excitation light intensity.

Note that the mere occurrence of significant band-gap PLE is already an indication of the high quality of the nanotubes, because even very low defect densities can completely quench the PLE of these one-dimensional emitters, as the exciton diffusion length in SWCNTs is as large as ~200nm.[14] This high quality is further confirmed by Raman spectroscopy (see section S4).

b. PLE maps of the various samples

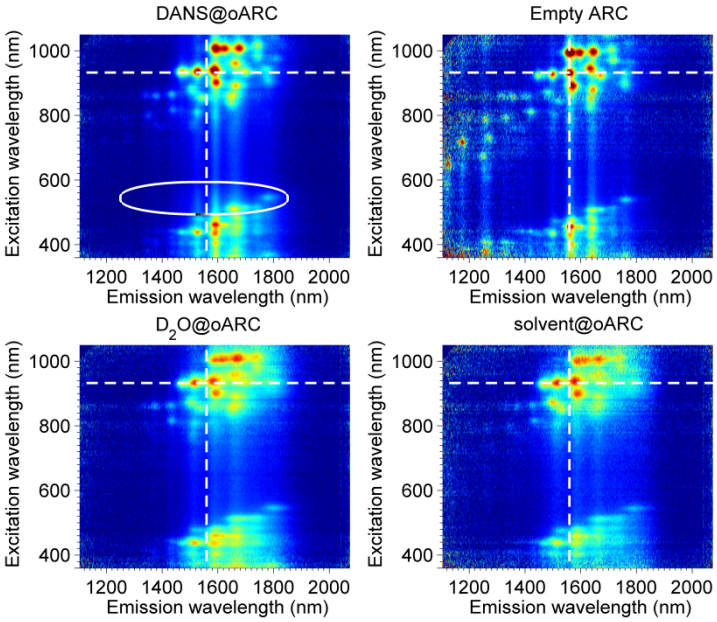

Figure S5. PLE maps for the ARC-samples. PLE maps for DANS@oARC and the corresponding empty ARC, D_2O@oARC and solvent@oARC. To visualize the electronic shifts, the position of the empty (12,7) nanotube is marked by the dashed lines. An additional band located at the excitation wavelength of DANS but at the emission wavelength of the SWCNTs for the DANS@oARC sample demonstrates energy transfer from DANS to the SWCNTs (highlighted by the ellipse). This energy transfer band is more clearly visualized in Fig. S7.

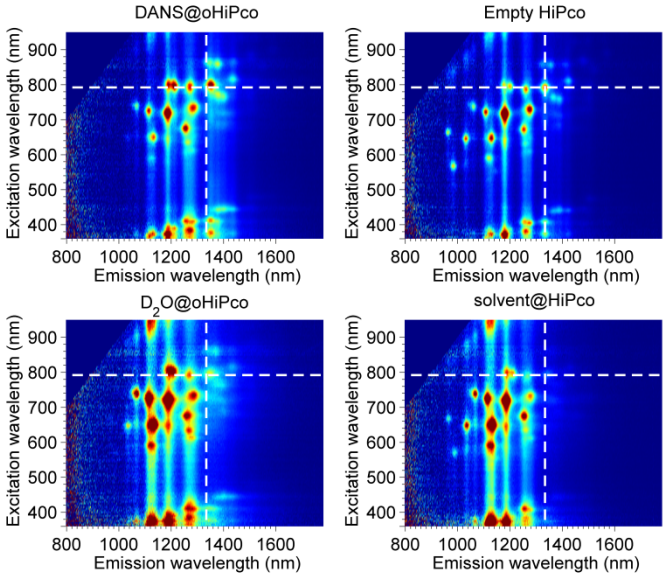

Figure S6. PLE maps for the HiPco samples. PLE maps for DANS@oHiPco and the corresponding empty HiPco, D_2O@oHiPco and solvent@HiPco. To visualize the electronic shifts, the position of the empty (9,7) tube is marked by the dashed lines. Here too, the energy transfer band is observed, for the largest diameters (emission above 1350nm; see also Fig. S7).

c. PLE difference maps: energy transfer

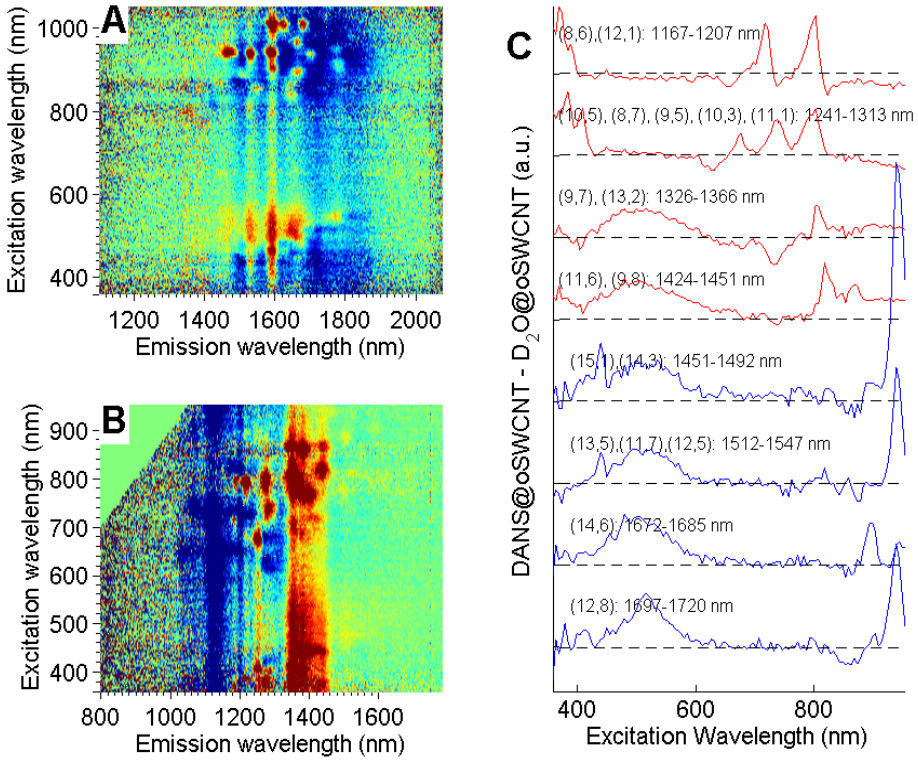

Figure S7. Energy transfer. a-b, Difference PLE maps obtained by subtracting the reference SWCNT (D_2O@oSWCNT) spectra from the DANS@oSWCNT spectra (**a** = ARC and **b** = HiPco). The energy transfer band is clearly visualized, as well as the onset of the energy transfer around 1350nm. **c**, Narrow 1D vertical slices from the difference PLE maps (ARC = blue, HiPco = red), representing the excitation spectra (including energy transfer) from a discrete subset of SWCNT chiralities. In this way, the energy transfer excitation band for these subsets of SWCNTs, i.e. the excitation band of the DANS molecules encapsulated in these specific SWCNTs, is obtained (selected emission wavelength ranges and corresponding SWCNT chiralities are indicated). For diameters smaller than the (9,7) and/or (13,2) tubes, no energy transfer is observed. The slices are normalized over intrinsic SWCNT PLE intensity in the specific ranges, showing very similar intensities of the energy-transfer for different SWCNT chiralities above the minimum diameter for filling. Small spectral changes of the energy transfer band can also be observed, indicative of different stacking of the encapsulated molecules in SWCNTs with different diameters.

d. Normalization of the PLE maps

When interpreting the 2D PLE difference maps (Figs 2f-g and S7a-b) it is important to note that the intensity of the energy transfer band depends strongly on the abundance (and photoluminescence [PL] efficiency) of the SWCNTs in the different samples. The intensity of the energy transfer band in these difference maps is thus modulated by the abundance of the SWCNTs for each specific emission wavelength. When taking the narrow vertical slices as in Fig. S7c, one can normalize the energy transfer band over the intrinsic SWCNT PLE intensity in that specific emission region, resulting in very similar intensities of the energy transfer band for the different SWCNTs above the minimal diameter for filling.

Instead of taking these selected vertical slices, one can also apply this normalization to the entire PLE maps, by normalizing the intensities for each emission wavelength over the intrinsic E_{22} PLE intensities of the SWCNTs at that emission wavelength. To define the E_{22} excitation range, we use the previously introduced[7] grid of constant diameter and chiral angle in the PLE maps (Fig. S8). These gridlines were derived using the empirical relations for the electronic transition wavelengths of empty SWCNTs[7], by treating diameter and chiral angle as continuous variables. At each emission wavelength, the intrinsic E_{22} PLE intensity over which to normalize is then given by the corresponding PLE intensity integrated over the excitation wavelength range between the two outer red lines of the grid (extended by 20nm on either side to account for spectral linewidths and minor spectral shifts ; Fig. S8). This normalization results in Figs 2h and S9.

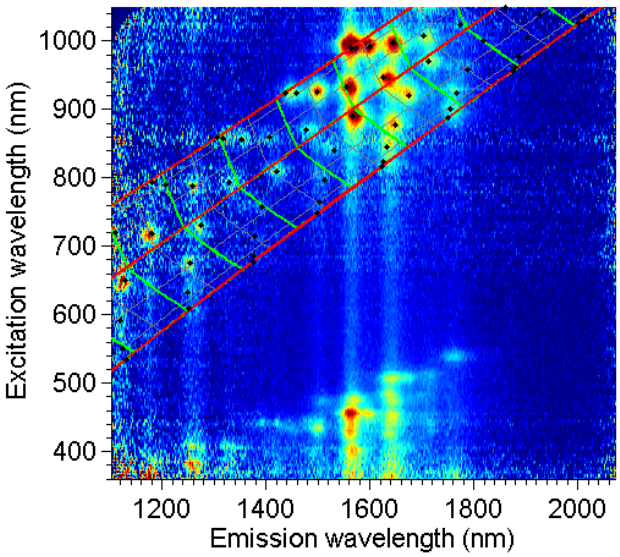

Figure S8. Example of the constant-diameter, constant chiral angle grid used for the normalization. PLE map of the empty ARC SWCNTs. Black dots are peak positions obtained by the empirical formula for empty SWCNTs derived in ref. [7]. Green lines are lines of constant diameter, using 0.1nm steps. Red lines are lines of constant chiral angle, with the middle line corresponding to α=0º and the two outer lines corresponding to α=30º for tubes with (n-m) mod 3=1 and 2, respectively. Normalization is then performed over the PLE intensity for each emission wavelength in between the two outer red lines of the grid (±20nm, see text).

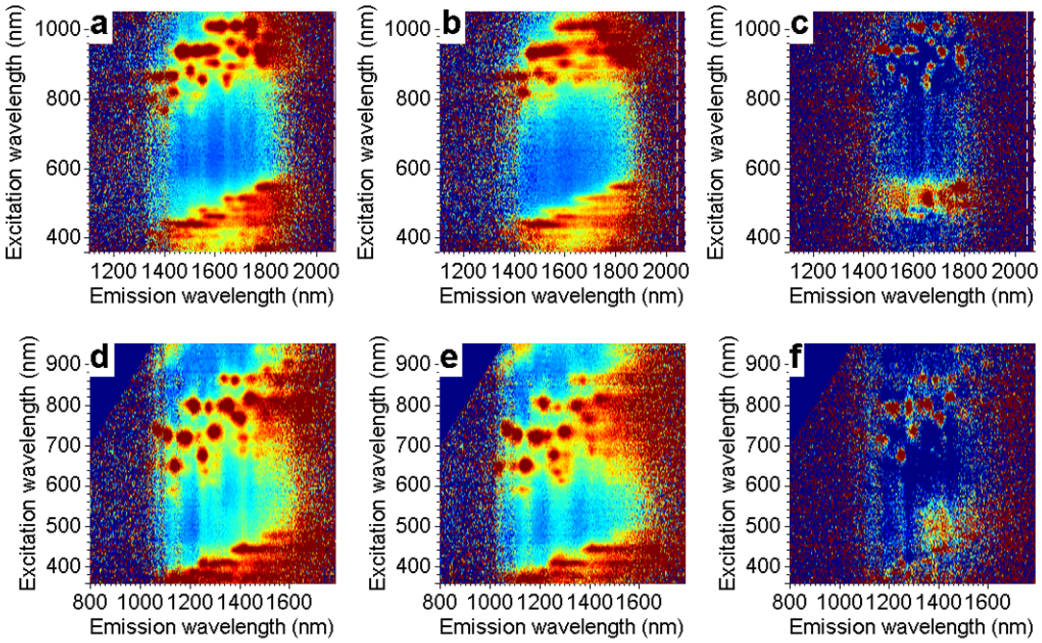

Figure S9. Normalized PLE maps. Normalized PLE maps from (**a**) DANS@oARC, (**d**) DANS@oHiPco, (**b**) D_2O@oARC and (**e**) D_2O@oHiPco. After normalization, the D_2O@oSWCNT map is subtracted from the DANS@oSWCNT map, thereby creating the difference maps for (**c**) oARC and (**f**) oHiPco SWCNTs. The energy transfer band is now clearly visible (at excitation wavelengths around 500nm), with a distinct onset at the emission wavelength of ~1350nm. Panels **c** and **f** were combined to create Fig. 2h, using oHiPco data for emission wavelengths below 1470nm, and oARC data above.

e. Two-dimensional fitting procedure

To accurately determine the shifts of the electronic transitions (i.e. E_{11} (emission) and E_{22} (absorption)) as a consequence of the dye encapsulation, an empirical model was developed to perform a two-dimensional fit of the PLE maps. This essential step is not straightforward and hardly discussed in the literature[15], as it is complicated by the presence of overlapping signals from multiple chiralities, with both excitonic and band-to-band transitions as well as phonon side bands. Therefore, especially the excitation line shape has not been modelled accurately before.

Our empirical model consists of the following:

- Emission profiles are fitted using a Voigt line shape, with transition wavelength λ_{11} and Lorentzian and Gaussian FWHM as fit parameters, from which also the overall linewidth $FWHM_{11}$ is derived.
- Excitation spectra are fitted taking into account both excitonic and band-to-band transitions:
  - E_{22} excitonic transitions are fitted using a Gaussian line shape, with peak position λ_{22} and linewidth $FWHM_{22}$.
  - Band-to-band transitions are modelled as $\propto 1/\sqrt{E-E_{22}}$, and convoluted with a Gaussian line shape with width $FWHM_{22}$, using the same peak position λ_{22} and linewidth $FWHM_{22}$ as the excitonic curve. These band-to-band contributions account for the broad tails of the excitation profiles, which are generally ignored in literature, but clearly observed in PLE maps as vertical stripes extending between the sharp excitonic transitions.

- The relative amplitudes of the band-to-band transitions to those of the excitonic transitions were fitted, but were taken to be the same for all chiralities in the sample. Since the band-to-band transitions are much weaker than the excitonic transitions (>20 times for ARC, and >4 times for HiPco, even at the peak of the convoluted van Hove singularity), and mainly needed only to model the tails far from resonance (where such contributions from multiple SWCNT chiralities accumulate), it is indeed reasonable to neglect the exciton binding energy (i.e. the small offset between band-to-band and excitonic transitions).
- Similarly also a band-to-band contribution from the first electronic transition (λ_{11}) was included in the fit of the excitation profiles (using the overall $FWHM_{11}$ from the emission profiles for the Gaussian convolution).
- For the HiPco SWCNTs, we furthermore implement a phonon side band, residing at approx. 0.2eV above the E_{22} excitation. The precise position was fitted, but was taken to be the same for each chirality and the linewidth was kept the same as the excitonic linewidth. To account for the changes of the relative amplitude of the phonon side band as a function of diameter (electron-phonon coupling decreasing steeply with diameter), a diameter-dependent (modelled through the emission wavelength) fitting parameter was included for the amplitude. For the ARC spectra, which only contain the larger diameters that do not show this phonon side band, the phonon side band was not included in the fit.

For two SWCNT chiralities, an additional side band at longer excitation wavelength ((8,6) SWCNT) or a splitting of the PLE peaks ((10,6) SWCNT) was observed. These anomalies were taken into account as an additional peak in the 2D fit, not used itself in the further interpretation, but required to allow other nearby peaks to be fitted reliably.
Figure S10 presents the fits for the DANS@oARC and DANS@oHiPco samples, showing an almost perfect reproduction of the experimental data. The resulting peak positions are plotted in Figure 3a (in comparison with the peak positions of the empty SWCNTs and solvent@oSWCNTs) and Figure S11 (in comparison with those from the empty SWCNTs and D_2O@oSWCNTs). For most of the DANS-filled SWCNTs an even larger red-shift than for the solvent- or water-filled SWCNTs is observed, indicating a stronger interaction of the excitons with the highly dipolar DANS molecules. Interestingly, some DANS-filled SWCNTs (in particular the (15,2) and (16,3) families, which have (n-m) mod 3 = 1) show a *less* red-shifted emission than the water-filled SWCNTs, which is possibly related to the different orientation of water dipoles compared to DANS dipoles (which are forced to be nearly parallel to the tube axis).

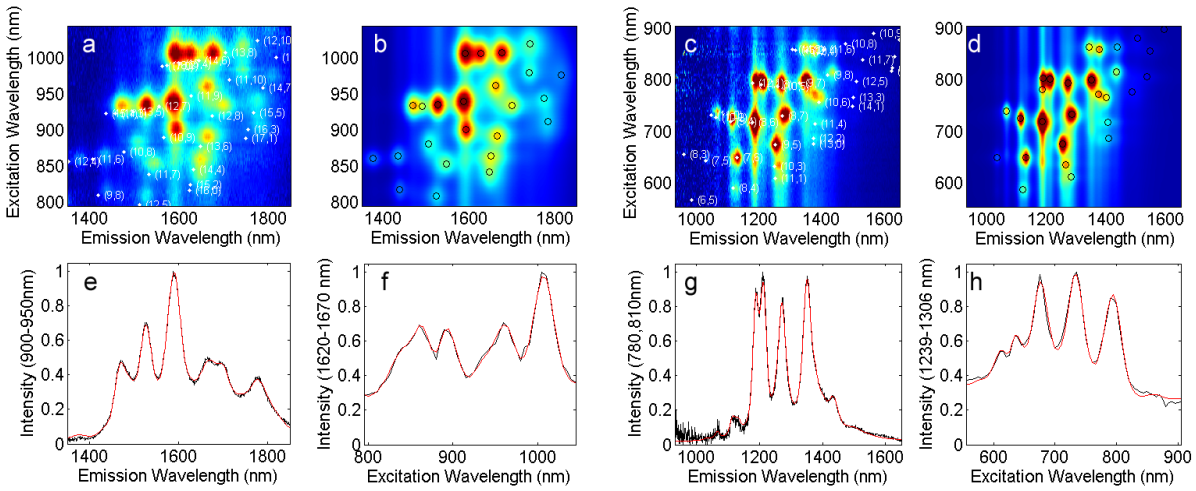

Figure S10. 2D PLE fits for DANS@oSWCNT. a-c, Experimental data of the DANS@oARC and DANS@oHiPco samples; **b-d**, 2D fits of these PLE maps; **e-g,** Horizontal slices of the experimental data (black) and fits (red); **f-h**, Vertical slices of the experimental data (black) and fits (red), showing that the model fits the experimental data extremely well.

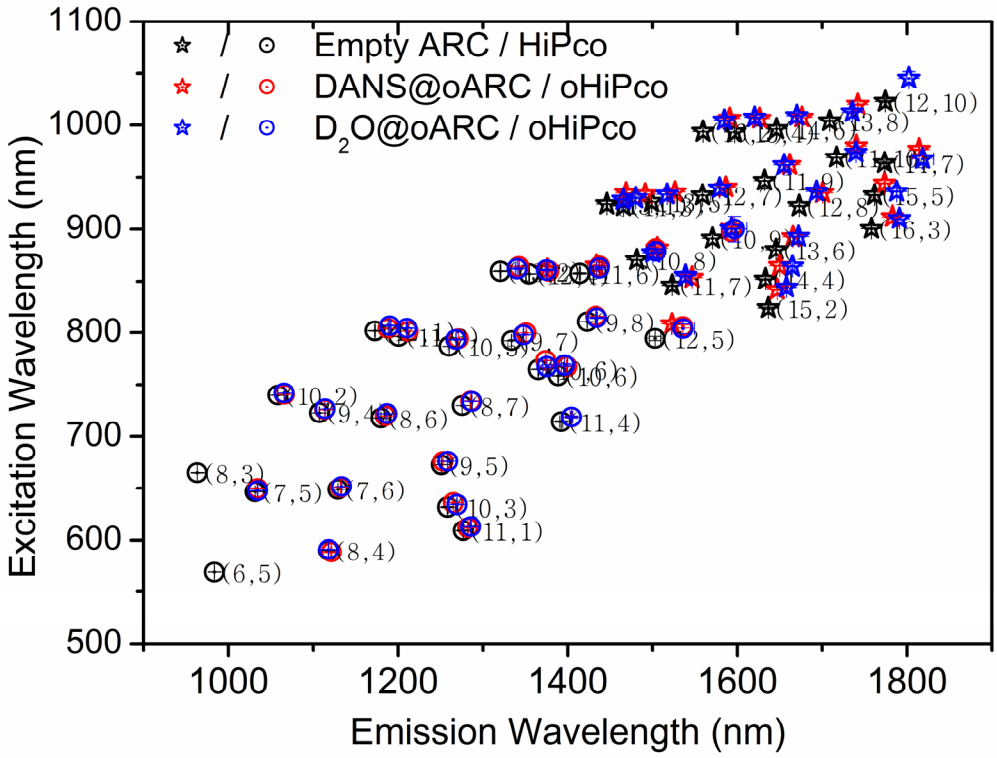

Figure S11. Comparison of PLE peak positions. Peak positions for the empty SWCNTs, DANS@oSWCNTs and D_2O@oSWCNT samples as obtained from the two-dimensional fits of the PLE maps.

f. Quenching of the DANS fluorescence

After encapsulation, the DANS fluorescence is nearly completely quenched, in agreement with very efficient energy transfer to the SWCNTs, which was also observed through the SWCNT emission in the PLE maps. To estimate the quenching factor, we measured the PL of DANS dissolved in toluene and THF (excitation at 447nm), and compared this to the PL of the DANS molecules in the DANS@oSWCNT samples. Samples were diluted (optical density less than 0.05 in a 1cm path length fused silica cell) to avoid effects of reabsorption. The PL arising from the SWCNTs and from the gradient medium was subtracted from the DANS@oSWCNT spectra. As such we find that the DANS fluorescence efficiency for DANS@oARC (DANS@oHiPco) is reduced by a factor of at least 670 (320) with respect to DANS in toluene; and 225 (100) with respect to DANS in THF. These values represent lower limits to the actual quenching factors because trace amounts of free DANS molecules or other impurities could easily explain the remaining fluorescence.

S4. Resonant Raman scattering spectroscopy (RRS)

a. Experimental details

Raman spectra were collected in backscattering geometry using a Dilor XY800 Triple spectrometer equipped with a liquid nitrogen cooled CCD detector. Several excitation wavelengths from three different lasers (Ar^+, Kr^+, and tunable Ti:sapphire laser) were used for resonant excitation in the electronic transitions of the SWCNTs.

b. Radial breathing modes (RBMs)

The frequency of the radial breathing mode (RBM) vibrations of SWCNTs is inversely proportional to their diameter, and is also very sensitive to interactions with their environment and to the encapsulation of molecules[1,5,7]. Previously we have shown that the RBMs of all SWCNTs exhibit a blue-shift after filling them with water, and that the relative amplitudes of RBM peaks corresponding to empty and filled SWCNTs allows for quantifying the fraction of filled SWCNTs[1,5,7]. Also the encapsulation of other solvent molecules (i.e. THF/DCM) and the DANS molecules can be studied by fitting the RBMs in the various samples (Figs S12-S16). First the peak positions of the empty and D_2O-filled SWCNTs were fitted simultaneously (using Lorentzian line shapes), since the empty sample might still contain a small fraction of water-filled tubes. As such the peak positions of the empty and water-filled tubes can be most accurately determined. Subsequently the solvent@oSWCNT spectra were fitted, which either contains tubes filled with water, or filled with other solvents (THF/DCM). Since the oSWCNTs samples contain a negligible amount of empty SWCNTs, the empty RBMs were omitted from the fits of the solvent@oSWCNT and DANS@oSWCNT spectra. For the large diameter tubes, no difference is observed between the D_2O-filled and solvent-filled SWCNTs. For the smaller tubes, significant differences can be observed, and thus these spectra were fitted using a combination of the known D_2O-filled SWCNT peak positions and linewidths and adding additional peaks (if necessary) to obtain a good fit. Finally, the DANS@oSWCNT spectra were fitted, taking into account the already known D_2O-filled and solvent-filled SWCNT peak positions determined by the previous fits, and only adding additional RBMs for those tubes where a fit with water- and solvent-filled SWCNT RBM peaks is not sufficient. In the overlapping diameter range of ARC and HiPco SWCNTs, the spectra of the ARC and HiPco

tubes were also fitted simultaneously to obtain a more accurate determination of the peak positions and linewidths.
The RBM frequency shifts that are presented in Figure 3d, are the RBM frequencies of the DANS-filled SWCNTs minus those of the solvent-filled SWCNTs. For chiralities for which no contribution from DANS-filled SWCNTs was observed, and an accurate fit of the RBM peaks was obtained without this additional contribution (i.e. those which are too narrow for DANS to enter), this shift is zero by definition, and the error bars presented for these SWCNTs are the error bars from the fits of the solvent-filled SWCNTs.
Assuming that the RRS cross-sections of the DANS-filled and solvent-filled SWCNTs are not drastically different (note that Figs. 3a and S11 show that the resonance conditions do not change much between solvent and DANS filling), we find that most SWCNT chiralities with diameters above the critical diameter are nearly 100% DANS-filled SWCNTs: For the (9,7) chirality (d = 1.088 nm) 72% (DANS@oARC sample) resp. 89% (in DANS@oHiPco) of the RBM signal corresponds to DANS-filled SWCNTs, while for all larger diameters (d ≥1.1nm, starting from the (13,2) SWCNT) filling percentages in the range of 88–100% are observed (on average 96% for diameters ≥1.1nm, or ~91% for the DANS@oARC sample as a whole, considering that based on optical absorption this sample contains about 4.5% of [non-filled] SWCNTs with d<1.1nm).

1) Excitation Wavelength = 790nm

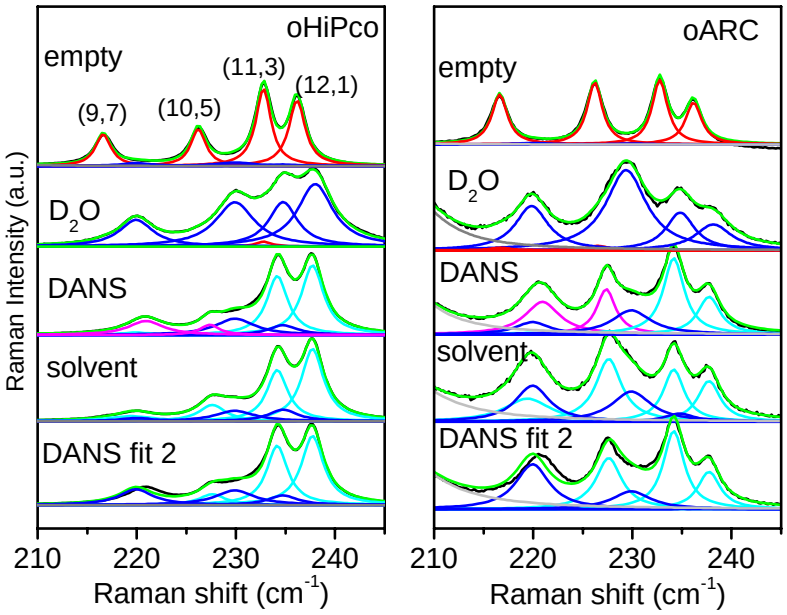

Figure S12. Fits (green) of the Raman spectra (black) of the oHiPco (left) and oARC (right) SWCNT samples excited at 790nm, by means of Lorentzian contributions from RBMs of empty (red), water-filled (blue), solvent-filled (cyan) and DANS-filled (magenta) SWCNTs (all spectra from both ARC and HiPco SWCNTs were fitted simultaneously with common position and linewidth parameters). The spectrum for the DANS-filled SWCNTs contains RBM peaks (corresponding to the (9,7) and (10,5) SWCNTs) that are clearly not fitted correctly by a combination of solvent-filled and water-filled SWCNTs only (DANS fit 2), and for which therefore an additional peak, corresponding to DANS-filled SWCNTs, is added.

2) Excitation Wavelength = 568.2nm

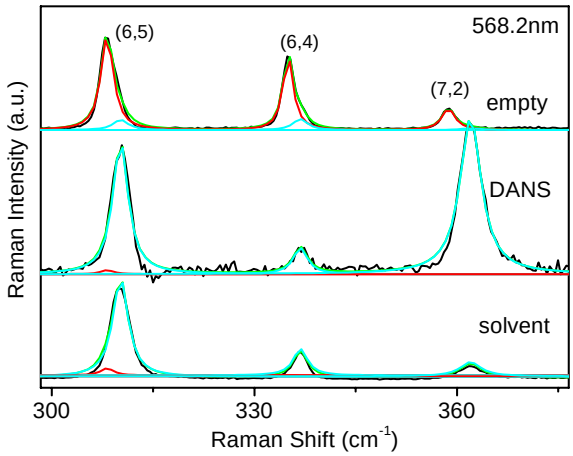

Figure S13. Fits (green) of the Raman spectra (black) of the empty HiPco, DANS@oHiPco and solvent@HiPco samples excited at 568.2nm, by means of Lorentzian contributions from RBMs of empty (red) and solvent-filled (cyan) SWCNTs. There is no difference in peak positions nor linewidths for the DANS@oHiPco samples with respect to the reference solvent@HiPco sample, indicating that the DANS molecules are not encapsulated in these narrow diameter SWCNTs.

3) Excitation Wavelength = 514.5nm

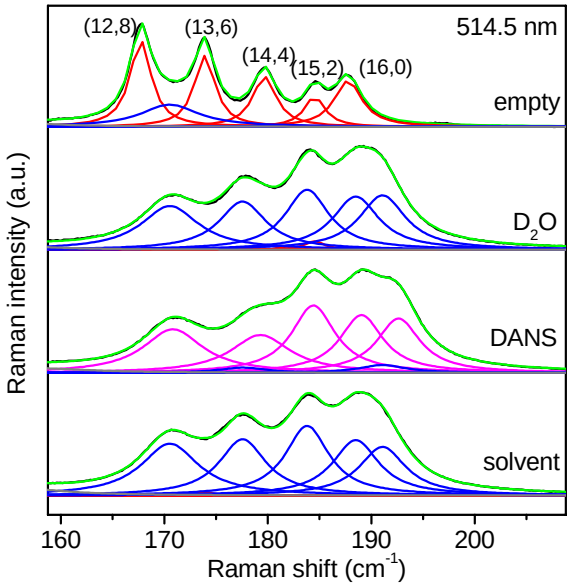

Figure S14. Fits (green) of the Raman spectra (black) of the empty ARC SWCNTs, the D_2O@oARC, DANS@oARC, and solvent@oARC samples excited at 514.5nm, by means of Lorentzian contributions from RBMs of empty (red), D_2O-filled (blue) and DANS-filled (magenta) SWCNTs. The solvent@oARC sample does not show differences with the D_2O@oARC sample indicating that during the solubilization the solvent molecules are exchanged by water-molecules. The fit shows that (among the SWCNT chiralities observed at this laser wavelength) the DANS@oARC sample contains almost exclusively SWCNTs that are filled with DANS molecules.

4) Excitation Wavelength = 725nm

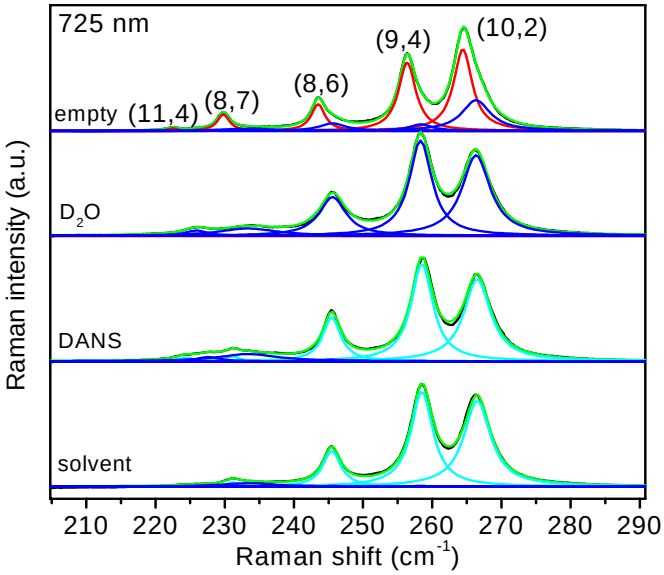

Figure S15. Fits (green) of the Raman spectra (black) of the empty HiPco, D_2O@oHiPco, DANS@oHiPco, and solvent@HiPco samples excited at 725nm, by means of Lorentzian contributions from RBMs of empty (red), D_2O-filled (blue) and solvent-filled (cyan) SWCNTs. The DANS@oHiPco sample does not show differences with the solvent@HiPco sample indicating that DANS molecules are not encapsulated in these small diameters, however solvent-molecules are encapsulated and show a different RBM peak position and linewidth than the D_2O-filled SWCNTs (also implying that the solvent molecules are not replaced by water in these smaller diameter SWCNTs).

5) Excitation Wavelength = 860nm

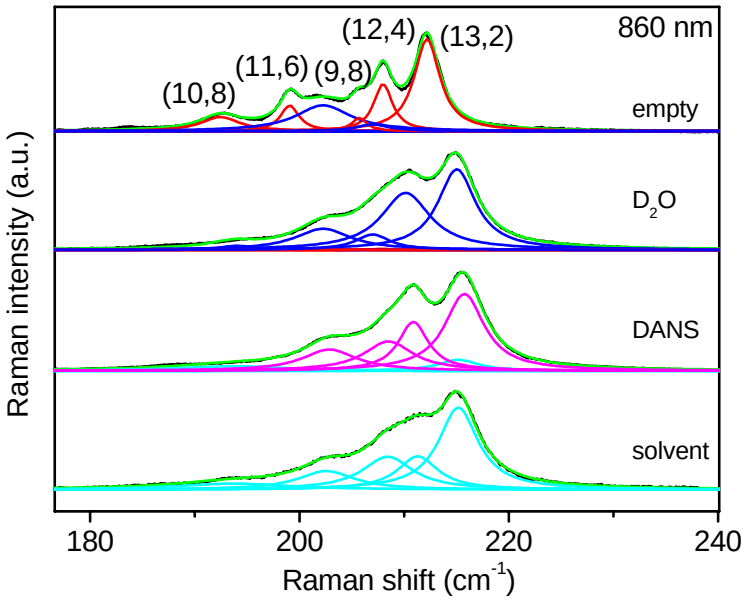

Figure S16. Fits (green) of the Raman spectra (black) of the empty ARC SWCNTs, the D_2O@oARC, DANS@oARC and solvent@oARC samples excited at 860nm, by means of Lorentzian contributions from RBMs of empty (red), D_2O-filled (blue) solvent-filled (cyan) and DANS-filled (magenta) SWCNTs. Again, the fit shows that the DANS@oARC sample contains mainly SWCNTs that are filled with DANS molecules.

c. Higher frequency modes

Additional evidence for the DANS-encapsulation is provided by RRS measurements of the higher frequency vibration modes, including both modes of the SWCNTs themselves and of the encapsulated molecules (Fig. S17). First of all, note that the opened oSWCNT do not show a significant defect induced D-band (e.g. black curve in Fig. S17, Raman spectrum of D_2O@oARC excited at 514.5nm: G/D ratio ≥220), indicating that even though the SWCNT ends are opened, the number of defects along the length of the tubes is extremely low (The D band is a symmetry forbidden mode, centred at 1350cm^{-1}, which is known to gain intensity when the SWCNT symmetry is broken by defects – such as missing or dislocated carbon atoms in the SWCNT wall, or covalent bonds formed to the SWCNT wall, changing the carbon atom's hybridisation – and in that case can be of comparable, or even larger, intensity as the G band[16]). For the DANS@oSWCNT sample, several additional bands originating from the encapsulated DANS-molecules can be observed: (i) 1150-1200cm^{-1} corresponding to C-C-stretch vibrations of the benzene ring and C-H bending vibrations; (ii) 1275-1350cm^{-1} corresponding to the NO_2 vibrations, (iii) 1550-1650cm^{-1} corresponding to the C=C-stretch vibrations and the NH_2 bending vibrations[17]. The inset of Figure S17 zooms in on these specific regions, after subtraction of the SWCNT Raman modes, and compares the vibrations of the encapsulated molecules with those of the molecules dissolved in methanol (for the solution spectra the fluorescence background was subtracted, while for the DANS@oARC no fluorescence background is observed (see section S3.f on quenching of the DANS PL)). Clear red-shifts and changes in relative intensities of the DANS vibrations can be observed due to the confinement inside the SWCNTs.

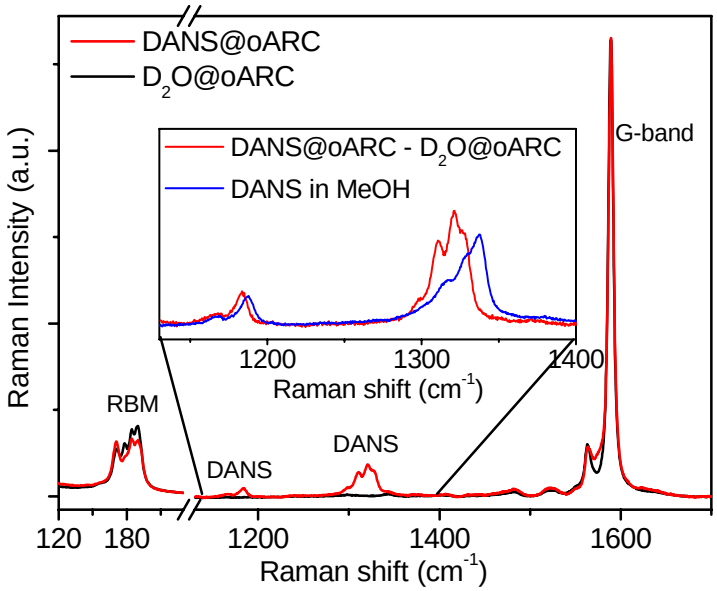

Figure S17: Raman spectra including the higher frequency range, excited at 514.5nm (hence also in resonance with the DANS molecules), for the DANS@oARC sample compared to the D_2O@oARC sample. RBMs and G-bands can be clearly distinguished and no significant defect-induced band can be observed (~1350cm^{-1}). The inset zooms in on the region of the C-C vibrations of the dye molecule, and compares them with those of the dye molecule dissolved in methanol.

S5. Hyper-Rayleigh scattering spectroscopy (HRS)

a. Experimental details

Hyper-Rayleigh scattering (HRS) is incoherent second harmonic light scattering occurring in disordered media[18,19]. Briefly, our highly sensitive and broadly wavelength-tunable HRS setup (described in detail in ref. [20]) consists of a Ti:Sapphire chirped-pulse regenerative amplifier (Spectra-Physics Spitfire) which is pumping a dual stage optical parametric amplifier (Spectra-Physics OPA-800CP, pulse duration ~2ps, repetition rate = 1kHz). Parallel detection of a narrow wavelength range around the second harmonic is achieved by use of a liquid nitrogen cooled CCD coupled to a spectrograph, enabling fast and complete correction for any multi-photon fluorescence which is then easily distinguished as a broad background[20-24]. With this unique setup, accurate HRS measurements are possible covering a broad wavelength range[20,25,26], throughout and beyond resonance with the DANS molecules. The high sensitivity in particular allows the pure solvent, which itself has a weak and accurately known β dispersion[20], to be used as the internal reference standard. The solutions were stirred during the measurement to continuously refresh the exposed molecules (limiting local heating and the effect of local decomposition, if any), and linear absorption spectra were recorded to check for decomposition.

For the HRS measurements on DANS in chloroform solution, the effective $|\beta_{ZZZ}|$ value of 0.49×10^{-30}esu for chloroform as determined in ref. [27] was adopted as internal calibration[20,23], and the dispersion of this value was taken into account as described before[20]. The calibrated HRS signal per DANS molecule S_c^{HRS} was calculated as

$$S_c^{HRS} = \frac{N_{CHCl_3}}{N_{DANS}}\left(\frac{S_{DANS}^{HRS} - S_{CHCl_3}^{HRS}}{S_{CHCl_3}^{HRS}}\right)\cdot\beta_{CHCl_3}^2, \qquad \text{(S1)}$$

were N is the number density. For the present case of free DANS molecules in solution, this signal is directly related to the molecular hyperpolarisability by $S_c^{HRS} = (\beta_{zzz}^{eff})^2$. Significant fluorescence was observed in all measurements involving detection at the long wavelength side of the DANS absorption band. In fact, at 1550nm no accurate measurement was possible for the free DANS molecules, due to a too strong fluorescence background (roughly 450 times the HRS signal). Samples were sufficiently diluted in order to keep the signal correction for reabsorption of the second harmonic light well below 5% (absorbance < 0.1/cm). Within good approximation, a single significant β tensor component along the z-axis (i.e. the direction of the elongated conjugated chain) was assumed for DANS[28-30]. The experimental error on the β values for DANS in chloroform, disregarding the systematic error on the reference value, is estimated to be ±5% (or 10% on the signals).

For the HRS measurements on the dye-filled SWCNTs, signals were recorded alternatingly for the pure surfactant solution (1% DOC in D_2O; signal $S_{solvent}^{HRS}$, for internal calibration, see below), the reference sample D_2O@oSWCNTs ($S_{D_2O@oSWNTs}^{HRS}$) and the isolated DANS@oSWCNT sample ($S_{DANS@oSWNTs}^{HRS}$). The signal from the empty SWCNTs themselves (i.e. $S_{D_2O@oSWNTs}^{HRS}$ minus $S_{solvent}^{HRS}$) was first subtracted from the DANS@oSWCNT signal (after rescaling the SWCNT signals (by less than 17%) for small differences in concentration, as determined by absorption spectroscopy). Then, from the remaining signal corresponding to the encapsulated DANS arrays in the

DANS@oSWNT hybrid assemblies, S_{hybrid}^{HRS}, and the signal of the 1% DOC in D_2O solution $S_{solvent}^{HRS}$, the calibrated HRS signal per DANS molecule S_c^{HRS} was calculated as

$$, S_c^{HRS} = \frac{N_{solvent}}{N_{DANS}} \left(\frac{S_{hybrid}^{HRS} - S_{solvent}^{HRS}}{S_{solvent}^{HRS}} \right) \cdot \beta_{solvent}^2 \qquad \text{(S2)}$$

were N is the number density. The concentration of DANS in the DANS@oSWCNT samples N_{DANS} was estimated from the DANS absorption band, and making use of the extinction coefficient of (28500±600)L·mol^{-1}·cm^{-1} for DANS in tetrahydrofuran solution (extinction coefficients in other solvents are in a similar range[9], with a standard deviation of only 8.7% for a wide range of polarities). For the internal calibration[20,23], the reference value $\beta_{solvent}$ is taken to be the effective β_{zzz} for water, which we previously calibrated extensively (and wavelength dependently) against chloroform[20]. Deuteration is not expected to have a significant effect on the β value, nor its dispersion, as the NLO response in this wavelength range is of electronic origin. Indeed, (i) we previously demonstrated this for (deuterated) dimethylformamide[20], (ii) we did not observe any significant vibrational contributions to β for an extensive series of solvents, including water[20], and (iii) also by other authors isotope effects have been found to be insignificant[31]. The contribution of DOC (at the concentration of 1% used) to the HRS signal was determined to be negligible: even for more than four times higher DOC concentrations, no significant increase of the HRS signal compared to pure D_2O was observed. Also the HRS contribution of the remaining density gradient medium ("NycoDenz"), present in the diluted SWCNT samples but not in the DOC/D_2O sample, was found to be negligible. We obtained an effective β_{zzz} value of only about 4.4×10^{-30}esu at 1220nm in D_2O for NycoDenz. This corresponds to a contribution to the signal of less than 1% at the concentrations of NycoDenz in the oSWCNT samples used for HRS, which were strongly diluted (typically more than an order of magnitude) with pure 1% DOC/D_2O to limit the corrections for absorption at the fundamental and second harmonic wavelength[20]. More in particular, absorbance at the second harmonic wavelength was kept well below 0.1/cm (keeping the signal correction well below 5%), and fundamental absorbance (excluding fundamental absorption of DOC/D_2O which does not need to be corrected for as it is identical for all samples and references) was typically kept below 0.06/cm (signal correction below 15%). A significant, but extremely broadband fluorescence background was observed for all SWCNT samples at all wavelengths, but in all cases the sharp HRS signal could still be accurately distinguished and was subtracted by means of a linear up to a quadratic fit (also thanks to the strong quenching of the DANS fluorescence in the DANS@oSWCNT samples, see section S3.f).

Chemical stability of the DANS@oSWCNT assemblies, as well as of the D_2O@SWCNT samples was found to be excellent: even the strongly diluted samples used for HRS showed no sign of decomposition after many months of storage (in line with the high stability of encapsulated β-carotene in ref. [3]). When exposed to the full power from the amplified pulsed laser system (pulse energy ~40μJ), significant photodecomposition of both the DANS@oSWCNT and the D_2O@SWCNT samples occurred (as evidenced from the absorption spectra; probably due to local heating), but no decomposition was observed at the reduced powers used for the HRS measurements (pulse energy ~1-4μJ near resonance and ~5-8μJ at the longest wavelengths). Finally, apart from the DANS-arrays inside the SWCNTs, also the (much weaker) HRS signal of the SWCNTs themselves showed significant, but very different,

wavelength dependence. The integrated HRS signals of the reference samples D_2O@oARC and D_2O@oHiPco respectively ranged from 1 to 4 and from 2 to 5 times the HRS signal of DOC/D_2O, increasing towards longer wavelengths.

The experimental error on the calibrated signal values, excluding the systematic error on the original reference standard chloroform[20,27], is estimated to be ±20% (corresponding to 10% error on the hyperpolarisability). These errors represent an estimate of the standard deviation obtained from multiple measurements (typically four per laser wavelength) at the different wavelengths, and also includes the error on other experimental parameters such as sample concentration, but excludes the systematic error on the original reference standard chloroform[20,27]. The relative error is taken constant for all data points (statistical errors are dominated by laser fluctuations rather than shot noise), and is representative for the variations seen in the outer wavelength ranges, even if smaller variation is often observed in the central wavelength range (where laser power and stability is highest), and is therefore a conservative estimate for most wavelengths. The choice for a fixed relative error was made because the number of independent measurements per wavelength is too small to determine reliable standard deviations for each data point separately.

b. Results

Wavelength dependent HRS measurements were first performed on DANS in chloroform

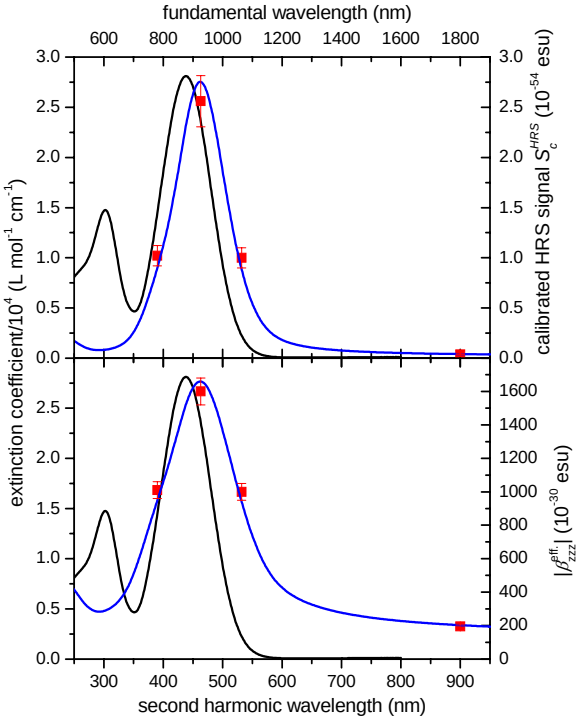

Figure S18. Tunable wavelength HRS data for the free DANS molecules. Experimental HRS data obtained for DANS in chloroform (red squares), shown together with the absorption spectrum of DANS in chloroform at the second harmonic wavelength (black curve). The blue curves represent the best fit of the homogeneously and inhomogeneously broadened vibronic (HIV) β dispersion model from ref. [37] (with G_{inhom}=1924cm^{-1}). The top panel shows the calibrated HRS signal per DANS molecule S_c^{HRS} (Eq. (S1)), while in the bottom panel the effective β_{zzz} values (=$\sqrt{S_c^{HRS}}$) are plotted.

solution (Fig. S18), showing a pronounced two-photon resonance in the region of the DANS absorption band. This resonance is red-shifted relative to the absorption maximum as observed previously for different NLO molecules[25,32-36], and explained by inhomogeneous broadening effects due to polar solvation[25]. The experimental, wavelength dependent β values for DANS were successfully modelled by means of the vibronic β dispersion model including both homogeneous and inhomogeneous broadening developed in ref. [37] (HIV model with G_{inhom}=1924cm^{-1}). This model (as opposed to the almost universally used two-level model[38] correctly describes both the resonantly enhanced data, including the red-shift, and the long wavelength tail, yielding an extrapolated signal S_c^{HRS} in the static limit of (0.0201±0.0020)×10^{-54}esu, corresponding to a static hyperpolarisability β_0 of (141±7)×10^{-30}esu for DANS.

The wavelength dependent HRS results obtained for the DANS@oSWCNT samples are summarized in Figs 4 and S19. A pronounced two-photon resonance associated with the encapsulated DANS molecules is again clearly observed for both the DANS@oARC and

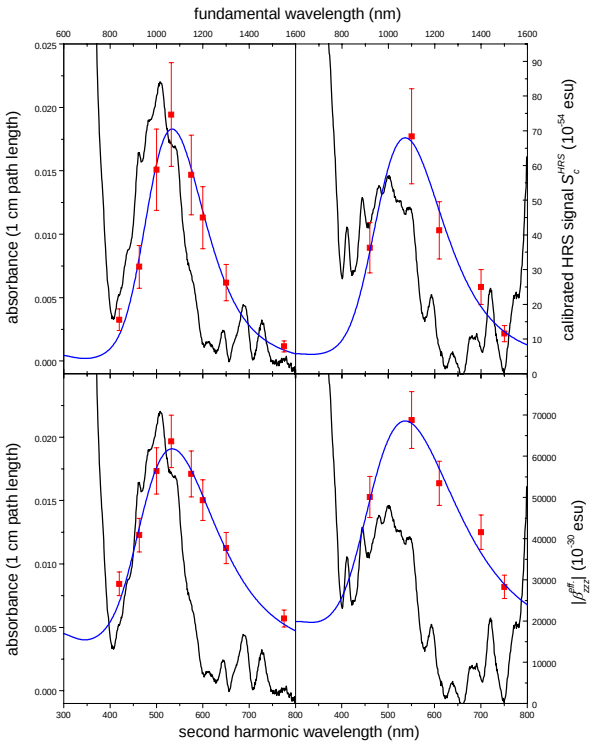

Figure S19. Tunable wavelength HRS data for the DANS@oSWCNT hybrid assemblies. Experimental HRS data (red squares) obtained for the DANS@oARC (left) and DANS@oHiPco (right) samples, shown together with the absorption spectra of the encapsulated DANS molecules (black curves). The blue curves represent the least squares fit to the data of our purely homogeneous vibronic-like (HV) model[17, 30]), including an additional red-shift (see text, $\lambda_{\text{eg,optimal}}$=525nm in the two cases, $\beta_{0,\text{array}}$=7660×10^{-30}esu and 9770×10^{-30}esu for DANS@oARC and DANS@oHiPco respectively). In the top two panels the calibrated HRS signal per DANS molecule (Eq. (S2)) is plotted, while in the two bottom panels these signals are converted to actual β values of the encapsulated DANS arrays (ordered domains) based on the S_c^{HRS} values at the static limit (see text).

DANS@oHiPco samples, and very large calibrated HRS signals S_c^{HRS} are obtained (Fig. S19, top panel). Note that here an even larger red-shift of the HRS maximum compared to the linear absorption maximum occurs, with a pronounced tail towards longer wavelengths. This can be understood as the DANS-filled SWCNT samples form a highly inhomogeneous system, consisting of nanotubes with different diameters and therefore a different stacking of the DANS molecules, which therefore exhibit different absorption and NLO behaviour. It is indeed expected that stackings closer to the ideal head-to-tail alignment, hence those with the largest contribution to β, also exhibit the more strongly red-shifted absorption. These effects are clearly more complicated than the simple inhomogeneous broadening due to solvation considered in the HIV model[37], which is hence not expected to yield a good description, but taking these peculiar stacking effects explicitly into account would introduce far too many free parameters. Therefore, we applied the HIV model while allowing an *ad hoc* additional red-shift (i.e. treating the transition wavelength λ_{eg} as one additional fit parameter), and found that a good overall fit could be obtained. This best fit was obtained in the homogeneous limit of this model (G_{inhom}=0; i.e. the purely homogeneous vibronic-like (HV) model[25,37], Fig. S19), which may seem surprising, but this simply means that the *ad hoc* red-shift alone (combined with the broad tails of the homogeneous model) succeeds in effectively accounting for the abovementioned stacking effects. The excellent fit again allows an accurate extrapolation of the HRS signals to the static limit, yielding values of $(1.09\pm0.22)\times10^{-54}$esu and $(1.39\pm0.28)\times10^{-54}$esu for the DANS@oARC and DANS@oHiPco samples respectively. The ratio of these values to that of the free DANS molecules ($(0.0201\pm0.0020)\times10^{-54}$esu) yields the effective average number of consecutively head-to-tail aligned molecules in the assemblies (~ average domain size, see section S6 below), i.e. ~54 and ~69 for the DANS@oARC and DANS@oHiPco samples respectively. This means that the hyperpolarisabilities of the entire assemblies (or of the ordered domains, if these are shorter than the SWCNTs) are respectively equal to 54 and 69 times the β of DANS in solution. This yields huge static values β_0 of 7660×10^{-30}esu (DANS@oARC) and 9770×10^{-30}esu (DANS@oHiPco), and extremely large peak β values of 63600×10^{-30}esu and 68800×10^{-30}esu respectively (Fig. S19, bottom panel). The highest values are obtained for the DANS@oHiPco sample. This is consistent with the fact that the DANS-filled tubes among the HiPco distribution have more ideal diameters to ensure a single molecular file, while some of the larger diameter tubes among the ARC SWCNTs might allow for a double file (possibly anti-parallel), or at least tilted stacking.

S6. Theoretical modelling of the polar alignment

In order to estimate the degree of alignment of the one-dimensional (1D) chain of molecules that could be expected theoretically, we devised a simple model accounting for dipole-dipole interactions, approximating each dipolar molecule as two point charges: We consider a finite chain of N molecules, placed on a lattice with lattice constant a, and the charges, $+q$ and $-q$, are located at distances l_+ and l_- from either sides of the lattice points (Fig. S20); while the currently used molecule DANS has the charges at either ends, i.e. $l_+ \approx l_-$, many other NLO molecules have a less symmetrical geometry, hence we start from this more general description). Due to the 1D confinement, each dipole i (i=1,..,N) is allowed to adopt one of only two possible orientations, described by the variable o_i: along the positive (o_i =+1) or negative (o_i =-1) x-direction.

The energy of a given configuration of the chain is then given by the Coulomb interaction energies E_{ij} between all pairs of dipoles (not counting the irrelevant interactions between both charges of the same dipole, which are independent of the molecular orientation), i.e.

$$H = \sum_{i=1}^{N-1}\sum_{j=i+1}^{N} E_{ij}$$
$$= \frac{q^2}{4\pi\varepsilon_0}\sum_{i=1}^{N-1}\sum_{j=i+1}^{N}\left(\frac{1}{(j-i)a+o_j l_+ - o_i l_+} + \frac{1}{(j-i)a-o_j l_- + o_i l_-} - \frac{1}{(j-i)a+o_j l_+ + o_i l_-} - \frac{1}{(j-i)a-o_j l_- - o_i l_+}\right) \quad \text{(S3)}$$

Based on this energy, the thermodynamic equilibrium of the chain order can be simulated numerically through Monte Carlo calculations using the Metropolis algorithm.

However, in the relevant regime with large ordered domains, it is more convenient to describe the state of the chain in terms of isolated defects (domain walls) separating ordered domains (Fig. S20). For sufficiently large domain sizes (low defect concentrations), we can neglect both defect-defect-interactions and interactions of defects with chain ends, such that the total energy (relative to the energy of the perfectly ordered "ground state") can be written simply as

$$H = n_d E_d \quad \text{(S4)}$$

where n_d is the number of defects, and E_d is the energy (heat of formation) to create one defect.

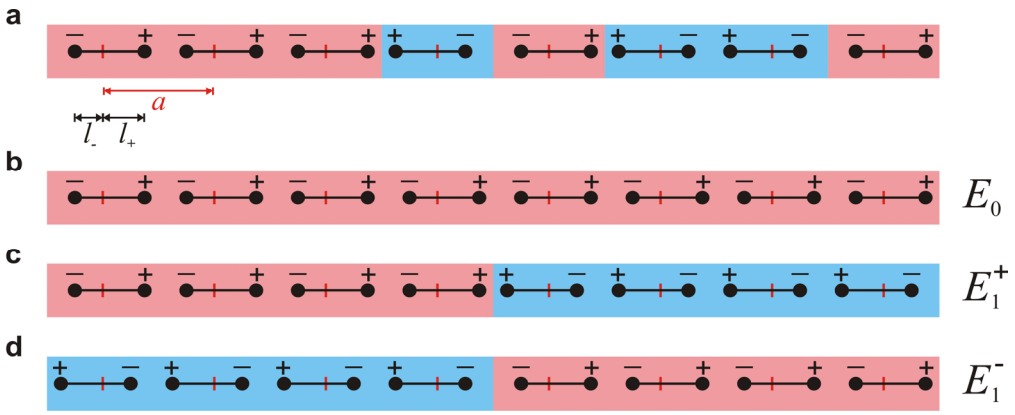

Figure S20. a, Definition of the model to describe the thermodynamics of the alignment of the 1D array of dipolar molecules. **b**, Perfectly ordered "ground state" of the chain and **c-d**, states with a single defect.

In fact, for the asymmetric case with $l_+ \neq l_-$, two inequivalent defect types exist, with neighbouring dipoles pointing towards each other or away from each other (Fig. S20), but it is a good approximation to set E_d equal to the average energy of both types (this can be understood as, neglecting end effects, a finite domain size requires both types of defects to occur alternatingly).

In a chain of N dipoles there are N-1 potential defect locations, and the probability p for a defect to occur at any given position is determined by Boltzmann statistics,

$$p = \frac{e^{-E_d/k_BT}}{1+e^{-E_d/k_BT}} \tag{S5}$$

where T is the temperature at which the chain was formed (synthesis temperature). Thus, the average number of defects in the chain is

$$\langle n_d \rangle = (N-1)\frac{e^{-E_d/k_BT}}{1+e^{-E_d/k_BT}} \tag{S6}$$

and the average domain size D (number of consecutive parallel aligned dipoles) is

$$\langle D \rangle = \frac{N}{1+\langle n_d \rangle} \tag{S7}$$

The total hyperpolarisability β_T of the chain is given in terms of the hyperpolarisability β of the individual molecules (which is assumed to be dominated by the diagonal tensor component along the long axis of the molecule) by

$$\beta_T = \sum_{i=1}^{N} o_i \beta \tag{S8}$$

Thus the calculation of the mean square hyperpolarisability $\langle \beta_T^2 \rangle$ as measured by HRS boils down to a calculation of the mean square polarization, i.e. of $\left\langle \left(\sum o_i\right)^2 \right\rangle$. To this end, we first calculate the correlation function $P_n = P(o_i = o_{i+n})$, i.e. the probability that two dipoles spaced by n lattice units have the same orientation, which can be expressed as the probability of having zero, or any other even number k of defects between these two dipoles (i.e. a sum of binomial distribution probabilities),

$$P_n = \sum_{\substack{k=0 \\ k\ even}}^{n} \binom{n}{k} p^k (1-p)^{n-k} \tag{S9}$$

where the binomial coefficient expresses the number of ways to distribute k defects over n potential defect sites. The sum over even k can be split into an average of the sum over all k, and

the analogous sum with alternating signs, both of which can be calculated using the binomial theorem (and the former summing to 1 as the binomial distribution is normalized) to yield

$$P_n = \frac{1}{2}\left(1 + (1-2p)^n\right) \tag{S10}$$

The mean square hyperpolarisability can then be calculated as

$$\left\langle \beta_T^2 \right\rangle = \beta^2 \left\langle \left(\sum_{i=1}^{N} o_i \right)^2 \right\rangle = \beta^2 \sum_{i=1}^{N}\sum_{j=1}^{N} \left\langle o_i o_j \right\rangle = \beta^2 \sum_{i=1}^{N}\sum_{j=1}^{N} \left[(+1)P(o_i = o_j) + (-1)P(o_i \neq o_j) \right] = \beta^2 \sum_{i=1}^{N}\sum_{j=1}^{N} \left[2P(o_i = o_j) - 1 \right] \tag{S11}$$

Note that in the above equation, β and β_T stand for the *zzz* components (where *z* is the axis of the 1D system) of the hyperpolarisability in the frame fixed to the molecule and DANS-filled nanotube respectively, and that the angle brackets "<>" only stand for the thermodynamic ensemble averaging over the different ordering states within the DANS-filled nanotube, not the orientational averaging which occurs in the HRS measurement in liquid solution, and which affects both the signal from the free molecules and from the DANS-filled nanotubes in the same way (e.g. scaling it by a factor of 6/35 in case of an unpolarised measurement[39], thus cancelling out in the enhancement factor of Eq. (S15).

Eq. (S11) can be worked out, making use of Eq. (S10), as

$$\left\langle \beta_T^2 \right\rangle = \beta^2 \sum_{i=1}^{N}\sum_{j=1}^{N} (1-2p)^{|i-j|} \tag{S12}$$

or, by substituting variables $\delta := |i-j|$,

$$\left\langle \beta_T^2 \right\rangle = \beta^2 \left[N + 2\sum_{\delta=1}^{N-1} (N-\delta)(1-2p)^{\delta} \right] \tag{S13}$$

which yields the closed-form analytic expression (through expression 0.113 in ref. [40])

$$\left\langle \beta_T^2 \right\rangle = \beta^2 \left[N + \frac{(1-2p)\left(2Np - 1 + (1-2p)^N\right)}{2p^2} \right] \tag{S14}$$

or, for the enhancement factor of the HRS signal compared to that of the same number of free molecules,

$$\frac{\left\langle \beta_T^2 \right\rangle}{N\beta^2} = 1 + \frac{(1-2p)\left(2Np - 1 + (1-2p)^N\right)}{2Np^2} \tag{S15}$$

where the defect probability p can be obtained via Eq. (S5) from the defect energy E_d, which is defined as the energy $E^{(1)}$ of a chain with a single defect minus the ground state energy $E^{(0)}$ of the

perfectly ordered chain. This could be calculated numerically from Eq. (S3) for a finite chain, but more elegantly, as we are considering isolated defects, we can take the limit of E_d for infinite chains. The perfectly ordered chain is described by o_i=+1 ($i \in \mathbb{Z}$) while the one with a single defect is defined as o_i=+1 for $i \geq 0$ and o_i=-1 for $i < 0$ (or *vice versa* for the other type of defect). The energy difference can then be expressed in terms of the pair interaction energies $E_{ij}^{(m)} = E_{j-i}^{(m)}$, where only pairs of dipoles interacting across the defect (hence depending only on the distance j-i) need to be considered:

$$E_d = \sum_{j=0}^{\infty} \sum_{i=-1}^{-\infty} E_{j-i}^{(1)} - E_{j-i}^{(0)} \tag{S16}$$

Grouping terms with the same distance j-i:=k this simplifies to

$$E_d = \sum_{k=1}^{\infty} k\left(E_k^{(1)} - E_k^{(0)}\right) \tag{S17}$$

Filling in the Coulomb interaction energies as in (S3) yields the required terms:

$$\begin{aligned} -kE_k^{(0)} &= \frac{q^2}{4\pi\varepsilon_0}\left(\frac{-2}{a} + \frac{k}{ak-(l_- + l_+)} + \frac{k}{ak+(l_- + l_+)}\right) \\ kE_k^{(1)\pm} &= \frac{q^2}{4\pi\varepsilon_0}\left(\frac{k}{ak \pm 2l_-} - \frac{k}{ak \pm (l_- - l_+)} + \frac{k}{ak \mp 2l_+}\right) \end{aligned} \tag{S18}$$

where the superscript index ± refers to the two types of defects (+ for the defect with dipoles pointing towards each other, which carries a positive charge). By combining terms on a common denominator and rearranging $kE_k^{(1)\pm}$ into partial fractions with denominators of order k^2, these expressions can be rewritten as

$$\begin{aligned} -kE_k^{(0)} &= \frac{q^2}{4\pi\varepsilon_0}\frac{2(l_- + l_+)^2}{a^3k^2 - a(l_- + l_+)^2} \\ kE_k^{(1)\pm} &= \frac{q^2}{4\pi\varepsilon_0}\left(\frac{4{l_-}^2}{a^3k^2 \pm 2a^2kl_-} \pm \frac{2(l_- - l_+)^2}{a^3k^2 \pm a^2k(l_- - l_+)} + \frac{4{l_+}^2}{a^3k^2 \mp 2a^2kl_+}\right) \end{aligned} \tag{S19}$$

Note that the sum over k of the *individual* terms in Eq. (S18) does not converge, but that of those in Eqs. (S19) does. Physically, this reflects the fact that charge-charge interaction energies (proportional to $1/r$) in an infinite chain of (net) charges diverge, but dipole-dipole interactions (falling off more rapidly, as $1/r^3$), constructed here from opposite point charges, do converge. Making use of the series expansion of the digamma function ψ (expression 6.3.16 in ref. [41],

$$\psi(1+z) = -\gamma + \sum_{k=1}^{\infty} \frac{z}{n(n+z)} \tag{S20}$$

and of the expansion in partial fractions of the cotangent function (expression 4.3.91 in ref. [41]),

$$\cot z = \frac{1}{z} + 2z\sum_{k=1}^{\infty}\frac{1}{z^2 - k^2\pi^2} \tag{S21}$$

the sums of Eqs. (S19) over k can be worked out analytically to yield the defect energy

$$E_d^{\pm} = \frac{q^2}{4\pi\varepsilon_0 a}\left[1 - \frac{l_- + l_+}{a}\pi\cot\frac{l_- + l_+}{a}\pi \mp \frac{2l_+}{a}\psi\left(1 \mp \frac{2l_+}{a}\right) \pm \frac{2l_-}{a}\psi\left(1 \pm \frac{2l_-}{a}\right) \mp 2\frac{l_- - l_+}{a}\psi\left(1 \pm \frac{l_- - l_+}{a}\right)\right] \tag{S22}$$

Taking the average of the energies of both types of defects, $E_d = (E_d^+ + E_d^-)/2$, and using the recurrence and reflection relations of the digamma function (expressions 6.3.5 and 6.3.7 in ref. [41]), this reduces to

$$E_d = \frac{q^2}{4\pi\varepsilon_0 a}\left[1 - \frac{l_- + l_+}{a}\pi\cot\frac{l_- + l_+}{a}\pi - \frac{l_+}{a}\pi\cot\frac{2l_+}{a}\pi - \frac{l_-}{a}\pi\cot\frac{2l_-}{a}\pi + \frac{l_- - l_+}{a}\pi\cot\frac{l_- - l_+}{a}\pi\right] \tag{S23}$$

which for the symmetrical case with $l_+ = l_- = l$ further simplifies to

$$E_d = \frac{q^2}{2\pi\varepsilon_0 a}\left(1 - \frac{2\pi l}{a}\cot\frac{2\pi l}{a}\right) \tag{S24}$$

Realistic model parameters q, a, and l for the NLO molecule DANS were obtained from quantum-chemical calculations at the Hartree-Fock level using the semiempirical Hamiltonian PM7[42,43]. First a calculation for an individual DANS molecule in vacuum was performed, yielding a dipole moment μ=9.142D (in line with results from *ab initio* calculations, giving dipole moments in the range 7.68–9.65D[30] and a dipole length 2l, taken to be the distance between both nitrogen atoms, of 12.27Å. From these two parameters, the effective point charge to create this dipole moment is derived: q=0.1564e. The lattice constant a was derived from a calculation of a head-to-tail DANS dimer in which the four nitrogen atoms were forced to stay on a straight line to simulate the 1D confinement, yielding a=16.88Å. Inserting these parameters into the above model yields the results shown in Fig. S21. Over the entire relevant temperature range, the analytical model for the low defect concentration regime is in good agreement with the full Monte Carlo simulation based on the full Coulomb interaction energy from Eq. (S3). Interestingly, the enhancement factor of the HRS signal of the dye-filled nanotubes compared to that of the same number of free molecules closely follows the average domain size itself. In other words, the finite domains are effectively (almost) equivalent to shorter, independent, i.e. randomly oriented dye-filled nanotubes. The HRS measurements can thus be used effectively to measure the average ordered domain size – no matter whether it is determined by nanotube length or by defects in the assembly. For the temperature used experimentally for the synthesis (339K, the boiling point of THF), the model yields an HRS enhancement factor of 43.3 (and 41.7 for the full simulation), reproducing the order of magnitude observed experimentally remarkably well, considering the simplicity of the model, and the steep dependence on temperature and other model parameters involved. For instance, relatively minor differences in dipole moment and spacing obtained by using the less accurate Hamiltonians AM1 or even PM6 (in fact, both of the most recently developed Hamiltonians, PM6 and PM7, have been shown to yield accuracies

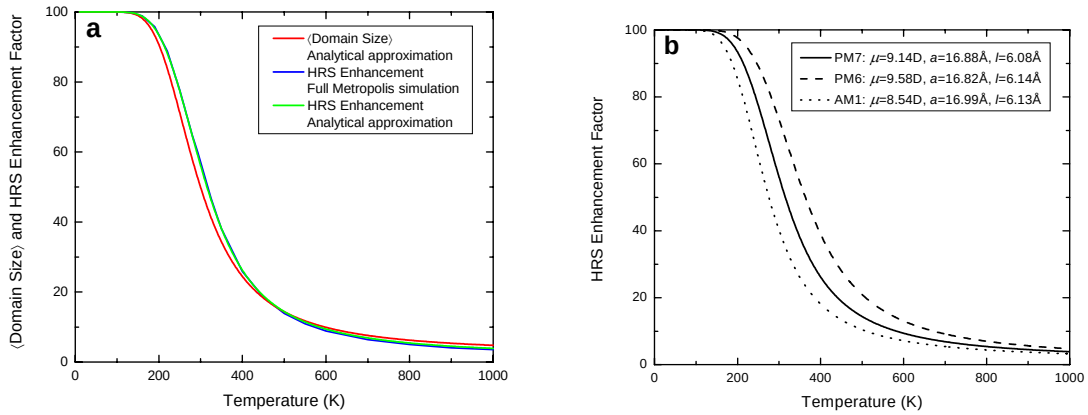

Figure S21. a, Results for the ordering of a 1D array of 100 DANS molecules from the model of Eqs. (S5),(S7),(S15) for the regime of low defect concentration, using the analytical expression (S24) for the defect energy, and comparison with the Monte-Carlo simulation based on the full Coulomb interaction energy of Eq. (S3), both using the model parameters from the quantum-chemical calculations with the PM7 Hamiltonian. Both the average size of the ordered domains, and the resulting enhancement of the HRS signal (compared to that from the same number of free DANS molecules) are plotted as a function of (synthesis) temperature. For each temperature, 20000 independent simulations were performed (400000 at the experimentally used synthesis temperature of 339K), with 600000 Metropolis steps each. Convergence was ensured by checking that simulations starting from a completely random initial state and from a completely ordered initial state (as well as from an initial state based on the low defect concentration limit approximation) yielded the same result (within a statistical error of ~0.18% at T=339K). Note that the analytical approximation is in good agreement with the full simulation over the entire relevant temperature range, and that the HRS enhancement closely follows the average domain size: Effectively, the domains act as shorter, independent, randomly oriented assemblies. **b**, Comparison of results (in the analytical approximation) using model parameters obtained from the more accurate Hamiltonian PM7, and two earlier semi-empirical Hamiltonians, AM1 and PM6, illustrating the critical dependence of the degree of ordering on relatively subtle changes in molecular dipole moment and spacing.

similar to or even better than DFT calculations at the hybrid B3-LYP level[43,44]), yield substantial differences in the degree of alignment (Fig. S21b). This is easily understood as the defect probability, and thus the average domain size, depends critically (through the Boltzmann factor in (S5)) on the Coulomb interaction energies, and thus equally critically on synthesis temperature. It is therefore to be expected that important further improvements will be possible through engineering of the molecules (dipole moment, spacing,...) and synthesis procedure. For instance, similarly sized zwitterionic NLO molecules can have several times higher dipole moments[45-47], and would thus allow the defect probability to be further reduced by multiple orders of magnitude, yielding domain sizes only limited by SWCNT length and dye purity.

S7. Solvent reaction field vs. electric field in the 1D array

The optical absorption spectra of free DANS molecules in solution show a pronounced red-shift with increasing solvent polarity (Fig. 2c). Despite the very apolar nature of the SWCNT internal channel, the DANS molecules in the SWCNTs show an even larger red-shift. This can be easily understood as the chromophores in the 1D array of dipoles in a head-to-tail arrangement experience an electric field due to the other dipoles which is comparable but even larger, and oriented in the same sense, as the reaction field experienced by the same dipole in a polar solvent (see below and Fig. S22). This reaction field is responsible for the solvatochromic shift: DANS is a typical dipolar chromophore with a positive solvatochromism[9], meaning that it has an even higher dipole moment in its excited state than in the ground state. Therefore, the excited state is stabilised (lowered in energy) more than the ground state by this polar environment (reaction field), resulting in a red-shift of the transition with increasing solvent polarity. To quantify the comparison of these electric fields in a polar solvent and in the 1D array, we calculated both using simple models.

The reaction field of a dipolar chromophore in a solvent can be obtained quite accurately from the well-known Onsager reaction field model, provided its generalization to an ellipsoidal cavity shape is used (even though the traditional model in which the molecule is assumed to occupy a spherical cavity is often used in literature, this is inappropriate for NLO chromophores, which are clearly elongated[45]). In this model, the solvent is described as a continuum with dielectric constant ε, and the chromophore is assumed to occupy an ellipsoidal cavity in this solvent, with its (point) dipole moment centered in the ellipsoid.[14] The reaction field due to the dielectric, polarized by the chromophore with dipole moment along the z-axis, is then given by

$$E_R = \frac{\mu}{4\pi\varepsilon_0}\frac{3}{r_x r_y r_z}\frac{A_z(1-A_z)(\varepsilon-1)}{\varepsilon+(1-\varepsilon)A_z} \qquad \text{(S25)}$$

where r_x, r_y, r_z are the semi-axes of the ellipsoidal cavity, and A_z is the so-called ellipsoidal shape factor given by

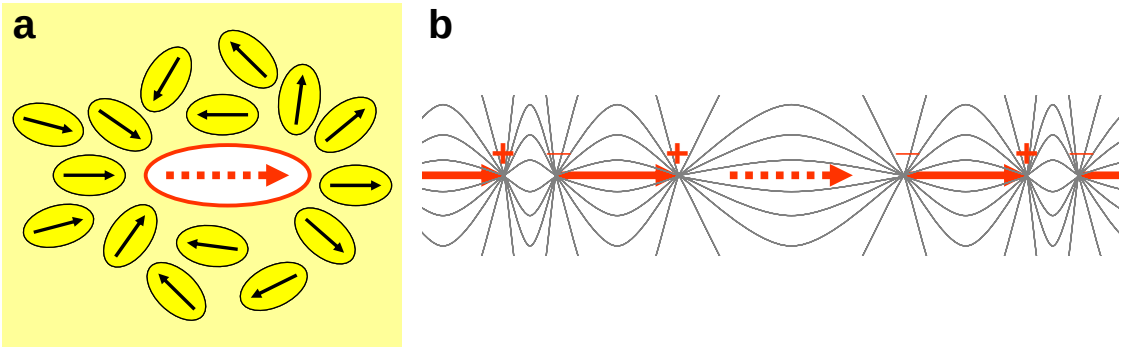

Figure S22. Schematic illustration of the electric fields experienced by the dipolar chromophores. **a**, In a polar solvent, the chromophore (red) experiences a reaction field due to the surrounding solvent molecules (black) which are polarized and oriented by the chromophore's electric dipole field. This reaction field can be well approximated as that of a dielectric continuum (yellow) surrounding the chromophore, in which the chromophore occupies an ellipsoidal cavity. **b**, In the 1D array of head-to-tail aligned dipolar chromophores, each chromophore also experiences an electric field due to the other chromophores, which is oriented in the same sense with respect to the dipole as its reaction field in a polar environment. This electric field can be calculated directly from the point-charge model defined in section S6.

$$A_z = \frac{r_x r_y r_z}{2} \int_0^\infty \frac{ds}{(s+r_x^2)^{1/2}(s+r_y^2)^{1/2}(s+r_z^2)^{3/2}} \quad \text{(S26)}$$

To obtain realistic cavity dimensions, we used the geometry of DANS optimised using the PM3 Hamiltonian,* and fitted an ellipsoid to the corresponding Van der Waals volume, yielding semi-axes r_x = 1.91Å, r_y = 3.43Å, r_z = 10.49Å. Inserting these in the model yields a reaction field of 8.33×10^8 V/m in DMSO ($\varepsilon = 48$; see Fig. S23 for other solvents).

The field experienced by a chromophore in the 1D head-to-tail array, due to all other dipoles in the array, can be calculated directly from the point charge model defined in the previous section. Using the model parameters from the PM7 calculation, this field, averaged over the length of the molecule (i.e. averaging along the z-axis from $-a/2$ to $a/2$), amounts to 9.49×10^8 V/m.

Thus the field acting on a DANS chromophore in the 1D head-to-tail array is indeed larger than the reaction field acting on the same dipolar chromophore in a very polar solvent such as DMSO, in line with the larger red-shift observed in the absorption spectra of DANS@oSWCNT compared to the free dye in solution (Fig 2c). The field in the 1D array will actually be even larger if one considers the additional influence of the (albeit small) polarity of the environment.

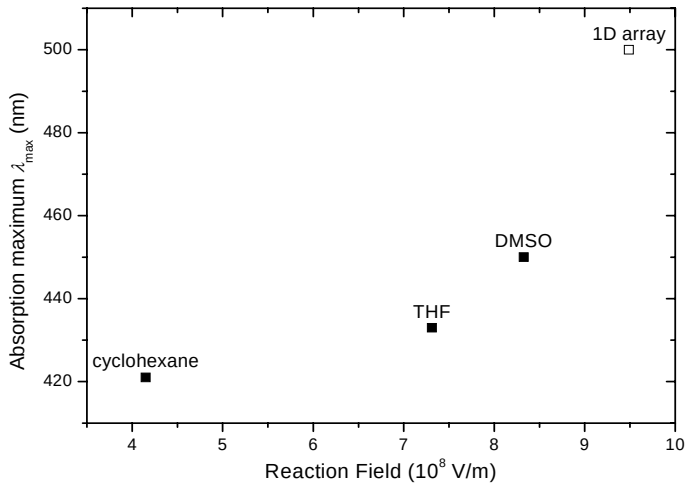

Figure S23. Experimental absorption maximum plotted as a function of the calculated electric fields experienced by the dipolar chromophores, in polar solvents (Onsager reaction field model with ellipsoidal cavity from equations S25-26; solid squares) and in the 1D head-to-tail array of dipolar chromophores (open square).

* Different quantumchemical methods yield very similar results. The PM3 geometry was chosen because it is more planar: The PM7 geometry is more twisted around the central vinylene link, which is expected to have very little effect on the reaction field, but lends itself less to fitting with an ellipsoid. Nevertheless, fitting the PM7 geometry instead yields an ellipsoid with very different rx/ry aspect ratio (r_x = 2.64Å, r_y = 2.91Å, r_z = 10.32Å), but very similar reaction field (8.39×10^8 V/m in DMSO), because the reaction field only depends on the ratio of the long axis (r_z, along the dipole moment) to the cross-section in the *xy*-plane.

References

1 Wenseleers, W. *et al.* Effect of water filling on the electronic and vibrational resonances of carbon nanotubes: Characterizing tube opening by Raman spectroscopy. *Adv. Mater.* **19**, 2274-2278, (2007).

2 Cambré, S. *et al.* Endohedral copper(II)acetylacetonate/single-walled carbon nanotube hybrids characterized by electron paramagnetic resonance. *J. Phys. Chem. C* **113**, 13505-13514, (2009).

3 Yanagi, K. *et al.* Highly stabilized *β*-carotene in carbon nanotubes. *Adv. Mater.* **18**, 437-441, (2006).

4 Yanagi, K. *et al.* Photosensitive function of encapsulated dye in carbon nanotubes. *J. Am. Chem. Soc.* **129**, 4992-4997, (2007).

5 Cambré, S. *et al.* Experimental observation of single-file water filling of thin single-wall carbon nanotubes down to chiral index (5,3). *Phys. Rev. Lett.* **104**, 207401, (2010).

6 Kim, U. J. *et al.* Raman and IR spectroscopy of chemically processed single-walled carbon nanotubes. *J. Am. Chem. Soc.* **127**, 15437-15445, (2005).

7 Cambré, S. & Wenseleers, W. Separation and diameter-sorting of empty (end-capped) and water-filled (open) carbon nanotubes by density gradient ultracentrifugation. *Angew. Chem. Int. Ed.* **50**, 2764-2768, (2011).

8 Arnold, M. S. *et al.* Sorting carbon nanotubes by electronic structure using density differentiation. *Nature Nanotechn.* **1**, 60-65, (2006).

9 Shin, D. M. & Whitten, D. G. Solvatochromic behavior of intramolecular charge-transfer diphenylpolyenes in homogeneous solution and microheterogeneous media. *J. Phys. Chem.* **92**, 2945-2956, (1988).

10 Wenseleers, W. *et al.* Efficient isolation and solubilization of pristine single-walled nanotubes in bile salt micelles. *Adv. Funct. Mater.* **14**, 1105-1112, (2004).

11 Streit, J. K. *et al.* Directly measured optical absorption cross sections for structure-selected single-walled carbon nanotubes. *Nano Lett.* **14**, 1530-1536 and references therein, (2014).

12 Choi, S. *et al.* An Explicit Formula for Optical Oscillator Strength of Excitons in Semiconducting Single-Walled Carbon Nanotubes: Family Behavior. *Nano Lett.* **13**, 54-58, (2012).

13 Lambin, P. Electronic structure of carbon nanotubes. *C. R. Physique* **4**, 1009-1019, (2003).

14 Oudjedi, L. *et al.* Metrological Investigation of the (6,5) Carbon Nanotube Absorption Cross Section. *J. Phys. Chem. Lett.* **4**, 1460-1464, (2013).

15 Rocha, J.-D. R. *et al.* Efficient spectrofluorimetric analysis of single-walled carbon nanotube samples. *Anal. Chem.* **83**, 7431-7437, (2011).

16 Dresselhaus, M. S. *et al.* Defect characterization in graphene and carbon nanotubes using Raman spectroscopy. *Philos. Trans. R. Soc. Lond., A* **368**, 5355-5377, (2010).

17 Moran, A. M. *et al.* Effects of a paracyclophane linker on the charge-transfer transition of 4-(Dimethylamino)-4‘-nitrostilbene. *J. Phys. Chem. A* **106**, 4928-4937, (2002).

18 Terhune, R. W. *et al.* Measurements of nonlinear light scattering. *Phys. Rev. Lett.* **14**, 681-684, (1965).

19 Clays, K. & Persoons, A. Hyper-Rayleigh scattering in solution. *Phys. Rev. Lett.* **66**, 2980-2983, (1991).

20 Campo, J. *et al.* Highly sensitive setup for tunable wavelength hyper-Rayleigh scattering with parallel detection and calibration data for various solvents. *Opt. Express* **17**, 4587-4604, (2009).

21 Stadler, S. *et al.* Problems associated with hyper-Rayleigh scattering as a means to determine the second-order polarizability of organic chromophores. *J. Phys. Chem.* **100**, 6927-6934, (1996).

22 Morrison, I. D. *et al.* Measurement of first hyperpolarizabilities by hyper-Rayleigh scattering. *Rev. Scient. Instr.* **67**, 1445-1453, (1996).

23 Goovaerts, E. *et al.* in *Handbook of Andvanced Electronic and Photonic Materials and Devices* Vol. 9 (ed Hari Singh Nalwa) Ch. 3, 127-191 (Academic Press, 2001).

24 Flipse, M. C. *et al.* The determination of first hyperpolarizabilities *β* using hyper-Rayleigh scattering: a caveat. *Chem. Phys. Lett.* **245**, 297-303, (1995).

25 Campo, J. *et al.* Accurate determination and modeling of the dispersion of the first hyperpolarizability of an efficient zwitterionic nonlinear optical chromophore by tunable wavelength hyper-Rayleigh scattering. *J. Phys. Chem. C* **112**, 287-296, (2008).

26 Campo, J. *et al.* First hyperpolarizability dispersion of the octupolar molecule crystal violet: multiple resonances and vibrational and solvation effects. *J. Am. Chem. Soc.* **132**, 16467-16478, (2010).

27 Kajzar, F. *et al.* Electric-field-induced optical second-harmonic generation in polydiacetylene solutions. *Phys. Rev. A* **36**, 2210-2219, (1987).

28 Oudar, J. L. Optical nonlinearities of conjugated molecules. Stilbene derivatives and highly polar aromatic compounds. *J. Chem. Phys.* **67**, 446-457, (1977).

29 Schweig, A. Calculation of static electric higher polarizabilities of closed shell organic π-electron systems using a variation method. *Chem. Phys. Lett.* **1**, 195-199, (1967).

30 Reis, H. *et al.* Comparison of the non-linear optical properties of a dimethylaminostilbene derivative containing a molybdenum mononitrosyl redox centre and of *p*,*p*'-dimethylaminonitrostilbene, calculated by ab-initio methods. *Phys. Chem. Chem. Phys.* **3**, 3901-3905, (2001).

31 Kaatz, P. *et al.* A comparison of molecular hyperpolarizabilities from gas and liquid phase measurements. *J. Chem. Phys.* **108**, 849-856, (1998).

32 Wang, C. H. *et al.* Measurements of the first hyperpolarizabilities of thiophene-based charge-transfer chromophores with hyper-Rayleigh scattering at 1064 and 1907 nm. *Chem. Phys.* **262**, 475-487, (2000).

33 Wang, C. H. *et al.* Hyper-Rayleigh scattering and frequency dependence of the first molecular hyperpolarizability of a strong charge-transfer chromophore. *J. Chem. Phys.* **119**, 6237-6244, (2003).

34 Robalo, M. P. *et al.* Synthesis, characterisation and molecular hyperpolarisabilities of pseudo-octahedral hydrido(nitrile)iron(II) complexes for nonlinear optics: X-ray structure of $[Fe(H)(dppe)_2(4\text{-}NCC_6H_4NO_2)][PF_6]\cdot CH_2Cl_2$. *Eur. J. Inorg. Chem.* **2006**, 2175-2185, (2006).

35 Otomo, A. *et al.* Key trade-offs for second harmonic generation in poled polymers. *Appl. Phys. Lett.* **69**, 1991-1993, (1996).

36 Hung, S. T. *et al.* Resonant Raman spectra and first molecular hyperpolarizabilities of strongly charge-transfer molecules. *J. Chem. Phys.* **123**, 144503, (2005).

37 Campo, J. *et al.* Practical model for first hyperpolarizability dispersion accounting for both homogeneous and inhomogeneous broadening effects. *J. Phys. Chem. Lett.* **3**, 2248-2252, (2012).

38 Oudar, J. L. & Chemla, D. S. Hyperpolarizabilities of the nitroanilines and their relations to the excited state dipole moment. *J. Chem. Phys.* **66**, 2664-2668, (1977).

39 Cyvin, S. J. *et al.* Theory of Hyper-Raman effects (nonlinear inelastic light scattering): selection rules and depolarization ratios for the second-order polarizability. *J. Chem. Phys.* **43**, 4083-4095, (1965).

40 Gradshteyn, I. S. & Ryzhik, I. M. *Table of integrals, series, and products*. 7 edn, Eq. 0.113 (Academic Press, 1980).

41 Abramowitz, M. & Stegun, I. A. *Handbook of mathematical functions with formulas, graphs, and mathematical tables*. 10 edn, 258-259 (Dover, 1972).

42 Gaufrès, E. *et al.* Giant Raman scattering from J-aggregated dyes inside carbon nanotubes for multispectral imaging. *Nature Photon.* **8**, 72-78, (2014).

43 Stewart, J. P. Optimization of parameters for semiempirical methods VI: more modifications to the NDDO approximations and re-optimization of parameters. *J Mol Model* **19**, 1-32, (2013).

44 Stewart, J. Optimization of parameters for semiempirical methods V: Modification of NDDO approximations and application to 70 elements. *J Mol Model* **13**, 1173-1213, (2007).

45 Szablewski, M. *et al.* Highly dipolar, optically nonlinear adducts of tetracyano-*p*-quinodimethane: synthesis, physical characterization, and theoretical aspects. *J. Am. Chem. Soc.* **119**, 3144-3154, (1997).

46 Beaudin, A. M. R. *et al.* Synthesis and properties of zwitterionic nonlinear optical chromophores with large hyperpolarizability for poled polymer applications. *Chem. Mater.* **18**, 1079-1084, (2006).

47 Kang, H. *et al.* Ultralarge hyperpolarizability twisted π-electron system electro-optic chromophores: synthesis, solid-state and solution-phase structural characteristics, electronic structures, linear and nonlinear optical properties, and computational studies. *J. Am. Chem. Soc.* **129**, 3267-3286, (2007).